



HAL
open science

X-Ray Amorphous Sulfur-Bearing Phases in Sedimentary Rocks of Gale Crater, Mars

R. J. Smith, S. M. Mclennan, B. Sutter, E. B. Rampe, E. Dehouck, K. L. Siebach, B. H. N. Horgan, V. Sun, A. Mcadam, N. Mangold, et al.

► **To cite this version:**

R. J. Smith, S. M. Mclennan, B. Sutter, E. B. Rampe, E. Dehouck, et al.. X-Ray Amorphous Sulfur-Bearing Phases in Sedimentary Rocks of Gale Crater, Mars. *Journal of Geophysical Research. Planets*, 2022, 127 (5), pp.e2021JE007128. <10.1029/2021JE007128>. <insu-03682336>

HAL Id: insu-03682336

<https://insu.hal.science/insu-03682336v1>

Submitted on 12 Oct 2022

HAL is a multi-disciplinary open access archive for the deposit and dissemination of scientific research documents, whether they are published or not. The documents may come from teaching and research institutions in France or abroad, or from public or private research centers.

L'archive ouverte pluridisciplinaire **HAL**, est destinée au dépôt et à la diffusion de documents scientifiques de niveau recherche, publiés ou non, émanant des établissements d'enseignement et de recherche français ou étrangers, des laboratoires publics ou privés.



HAL Authorization

1 **X-ray amorphous sulfur-bearing phases in sedimentary rocks of Gale crater, Mars**

2
3 **R. J. Smith^{1*}, S. M. McLennan¹, B. Sutter², E. B. Rampe³, E. Dehouck⁴, K. L. Siebach⁵, B.**
4 **H. N. Horgan⁶, V. Sun⁷, A. McAdam⁸, N. Mangold⁹, D. Vaniman¹⁰, M. Salvatore¹¹, M. T.**
5 **Thorpe¹², and C. N. Achilles⁸**

6 ¹Department of Geosciences, SUNY Stony Brook, Stony Brook, NY 11794, USA

7 ²Jacobs JETS at NASA Johnson Space Center, Houston, TX 77058, USA

8 ³Astromaterials Research and Exploration Science Division, NASA Johnson Space Center,
9 Houston, TX 77058, USA

10 ⁴Univ Lyon, UCBL, ENSL, UJM, CNRS, LGL-TPE, F-69622, Villeurbanne, France

11 ⁵Earth, Environmental and Planetary Sciences, Rice University, TX 77005, USA

12 ⁶Department of Earth, Atmospheric, and Planetary Sciences, Purdue University, West Lafayette,
13 IN 47907, USA

14 ⁷Jet Propulsion Laboratory, California Institute of Technology, Pasadena, CA 91109, USA

15 ⁸NASA Goddard Space Flight Center, Greenbelt, MD 20771, USA

16 ⁹Laboratoire de Planétologie et Géodynamique, UMR6112, CNRS, Université de Nantes, France

17 ¹⁰Planetary Science Institute

18 ¹¹Department of Astronomy and Planetary Science, Northern Arizona University, Flagstaff, AZ,
19 86011, USA

20 ¹²Texas State University, JETS, at NASA Johnson Space Center, Houston, TX 77058, USA

21
22 *Corresponding author: Rebecca Smith (rebecca.j.smith@stonybrook.edu)

23 **Key Points:**

- 24 • A large percentage of the bulk SO₃ in Gale crater sedimentary rocks is in the X-ray
25 amorphous state (20-90%).
26 • X-ray amorphous S-bearing phases are likely mixtures of Mg, Fe, Ca and other cation
27 sulfates present as cement and in diagenetic features.
28 • In situ detections of X-ray amorphous SO₃ likely contribute to orbital spectral detections
29 of sulfates in lower Mount Sharp.
30

31 **Abstract**

32 The Curiosity rover in Gale crater is investigating the transition from the “clay-bearing
33 unit” to the younger “sulfate-bearing” unit, which likely reflects a major aridification of the
34 Martian climate. To fully understand this transition, we must characterize the sulfur-bearing
35 phases encountered below it. The rocks below the transition have mostly crystalline Ca-sulfates
36 with minor Fe-sulfates, and often have some fraction of their bulk SO₃ in the X-ray amorphous
37 state with a poorly constrained nature. Here, we characterize the abundances and compositions of
38 the X-ray amorphous sulfur-bearing phases in 19 drill samples using mass balance calculations,
39 as well as evolved SO₂ gas measured by the SAM instrument for a subset of 5 samples. We find
40 that ~20-90 wt% of a sample’s bulk SO₃ is in the X-ray amorphous state and that X-ray
41 amorphous sulfur-bearing phase compositions are consistent with mixtures of Mg-S, Fe-S, and

42 possibly Ca-S phases, likely sulfates or sulfites. These materials reside in the bedrock, perhaps as
43 cementing agents deposited either with the detrital sediments or during early diagenesis, and in
44 diagenetic alteration halos likely deposited after lithification during late diagenesis. Many rocks
45 have large fractions of X-ray amorphous Mg-S phases, possibly highly soluble Mg-sulfates,
46 suggesting negligible fluid flow through the bedrock post-Mg-sulfate deposition. X-ray
47 amorphous sulfur-bearing materials likely contribute to orbital spectral detections of sulfates, and
48 so our results help form multiple hypotheses to be tested in the sulfate unit and are important for
49 understanding the evolution of the Martian surface environment at Gale crater.

50

51 **Plain Language Summary: (should be 200 words)**

52 The Curiosity rover in Gale crater, Mars is investigating a mineral transition observed
53 from orbit – older clay-rich to younger sulfur-rich rocks - that likely reflects a change from a
54 wetter to a drier Martian climate. Many of the sedimentary rocks investigated by the rover below
55 the mineral transition have X-ray amorphous sulfur-bearing phases that are poorly constrained.
56 To fully appreciate the significance of the transition to more sulfate-rich rocks, we must
57 understand the abundance and compositions of the X-ray amorphous sulfur-bearing phases
58 present below the transition. Here, we investigate the X-ray amorphous sulfur-bearing phases at
59 19 drill sites below the transition. We find that most rocks have large fractions of X-ray
60 amorphous sulfur-bearing phases that are likely mixtures of Mg-, Fe-, and possibly Ca-sulfates
61 or sulfites. In some rocks, X-ray amorphous sulfur-bearing phases might have precipitated from
62 solutions delivered to the lake early on and could be cementing sediment grains. In other
63 locations, X-ray amorphous sulfur-bearing phases are associated with zones where fluids altered
64 the rocks long after they were cemented. These results help form multiple hypotheses to be tested
65 in the sulfate-rich rock unit and are important for understanding the evolution of the Martian
66 surface environment at Gale crater.

67

68 **1 Introduction:**

69 One reason why the Mars Science Laboratory (MSL) mission was sent to Gale crater,
70 Mars was because orbital observations indicated that the central mound, Aeolis Mons, comprises
71 relatively flat-lying layered rocks that transition from stratigraphically lower (older) rock units
72 with clay/sulfate mineral spectral signatures to stratigraphically higher (younger) rock units with
73 sulfate/oxide spectral signatures (Milliken et al., 2010). This spectrally significant clay-sulfate
74 mineral transition has been noted in other locations on Mars (e.g., Bibring et al., 2006; Carter et
75 al., 2013) and is thought to preserve a period of global scale climate change in Mars' history
76 from a wetter to a more arid climate, possibly leading ultimately to the inhospitable conditions
77 found on the surface today (Bibring et al., 2006). To fully appreciate the nature, extent and
78 implications of this transition, it is important to “ground truth” the observation by investigating
79 the textures and chemistry of the sulfur-bearing mineral phases along the rover traverse and into
80 the mineralogical transition.

81 A range of sulfur-bearing mineral compositions has been observed in the sedimentary
82 rocks examined by the *Curiosity* rover. To date, the Chemistry & Mineralogy (CheMin) X-ray
83 diffractometer (XRD) (Blake et al., 2012) has detected mostly Ca-sulfates (gypsum, bassanite,
84 and anhydrite) with Fe-sulfates (jarosite) detected in relatively low abundances in some locations
85 (Vaniman et al., 2018; Rampe et al., 2020a). Notably, sulfides have not been identified above the
86 CheMin detection limit ($> \sim 1$ wt%) in any sample. The Sample Analysis at Mars (SAM)

87 instrument (Mahaffy et al., 2012) cannot detect Ca-sulfates, but SAM evolved gas analyses
88 (EGA) for most drill sites indicate SO₂ release temperatures and peak shapes consistent with Fe-
89 and Mg-sulfur-bearing materials. Additionally, EGA SO₂ traces and isotopic compositions show
90 that most samples have oxidized S-bearing phases such as sulfates and sulfites with reduced
91 sedimentary sulfides being important SO₂ contributors at only two locations (Franz et al., 2017).
92 These observations indicate mostly oxidizing conditions during the deposition of the sulfur-
93 bearing phases and the lack of detection of Mg-sulfates or sulfites (and in some cases Fe-
94 sulfates) by CheMin indicates that these phases are either mixtures of crystalline phases present
95 below CheMin detection limits and/or X-ray amorphous in nature.

96 X-ray amorphous phases are materials that either completely lack crystal structure
97 (amorphous) or do not have sufficient consecutive planes of atoms to create detectable peaks in
98 the X-ray diffraction patterns (Klug and Alexander, 1974). X-ray amorphous sulfur-bearing
99 materials are not common geologic materials on Earth. Hypotheses for these phases on Mars
100 include amorphous, nano-, or poorly crystalline sulfates formed through dehydration under
101 current Martian surface conditions or as precursors to crystalline sulfates (e.g., Vaniman et al.,
102 2004; Vaniman and Chipera, 2006; Wang et al., 2009; Sklute et al., 2015, 2018; Wang, Y. et al.,
103 2012), sulfate anions adsorbed onto X-ray amorphous weathering products (e.g., allophane,
104 ferrihydrite) (e.g. Rampe et al., 2016), and S-bearing phase inclusions in glass (McAdam et al.,
105 2014; Sutter et al., 2017). Sulfur-bearing phase properties (e.g., abundance, crystallinity,
106 composition) can be linked to environmental conditions such as relative humidity (RH), pH,
107 oxidation state, and salinity, and so constraining these properties can help inform on the
108 environments and processes that formed them.

109 Here, we use bulk X-ray amorphous component compositions calculated by Smith et al.
110 (2021) and detailed SAM evolved SO₂ gas analyses to compare the abundances and
111 compositions of the X-ray amorphous sulfur-bearing phases in most of the Gale crater rocks
112 examined by CheMin below the mineral transition detected from orbit. These results are then
113 used to speculate on the timing of deposition and their formation conditions. One of our findings,
114 that between 20 and 90 wt% of a sample's bulk SO₃ is in the X-ray amorphous state, highlights
115 the importance of this study as this observation indicates that large fractions of the sulfur-bearing
116 phases present below the spectrally significant mineral transition have not been characterized.
117 We discuss how these phases can allow us to better appreciate the geologic significance of the
118 mineral transition and increase our understanding the history of water in Gale crater in general.

119

120 **2 Background**

121 2.1 Geologic Context

122 As of sol 2300 (January 24, 2019; a sol is a Martian day, numbered from the first sol of
123 any mission), the *Curiosity* rover has worked its way up the slopes of Aeolis Mons, investigating
124 ~380 vertical meters of the sedimentary rocks that make up the basal part of this ~5 km high
125 topographic feature (e.g., Grotzinger et al., 2014, 2015). The Gale crater impact event has been
126 dated to between ~3.6 and 3.8 Gy ago during the late Noachian/early Hesperian epochs
127 (Thomson et al., 2011), and it is possible that the entire crater was filled with fluvial, lacustrine,

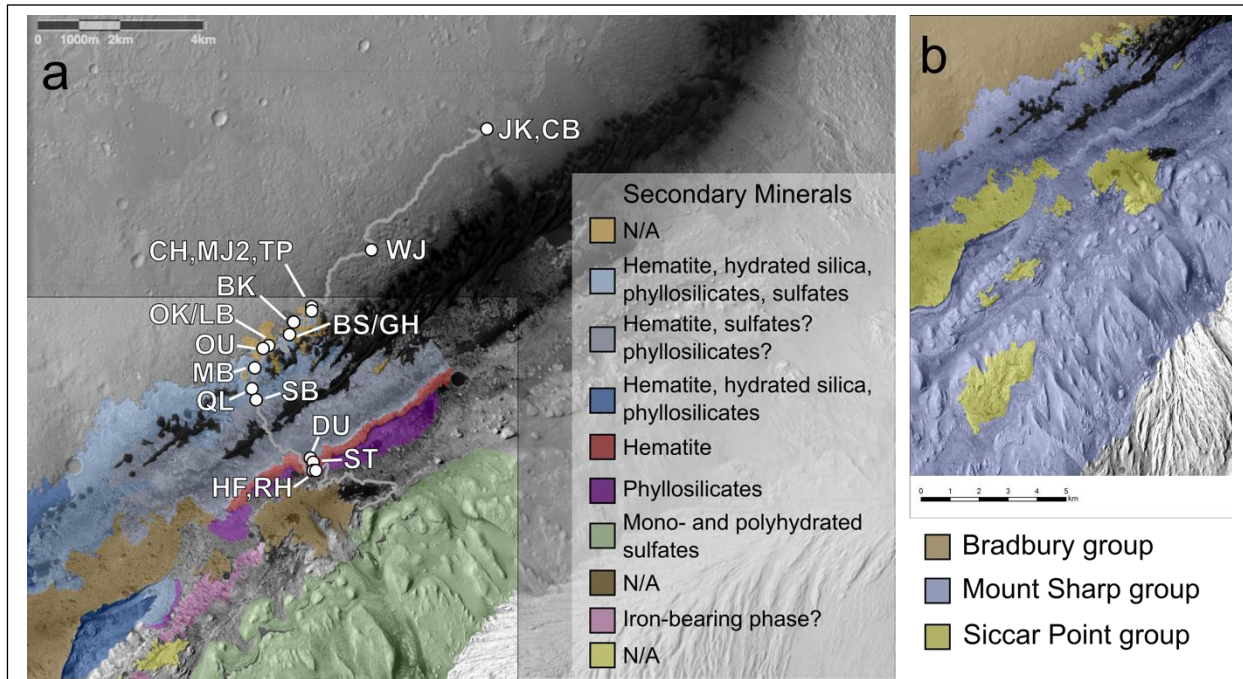


Figure 1. Modified from Fraeman et al. (2016). (a) Rover traverse (grey line) and drill hole locations (white dots) shown in context with major spectral units and interpreted secondary mineralogy as defined by Fraeman et al. (2016). (b) Figure from Fraeman et al. (2016) showing stratigraphic groups discussed in this study. Drill holes: JK–John Klein, CB–Cumberland, WJ–Windjana, CH–Confidence Hills, MJ–Mojave, TP–Telegraph Peak, BK–Buckskin, OU–Oudam, MB–Marimba, QL–Quela, SB–Sebina, DU–Duluth, ST–Stoer, HF–Highfield, RH–Rockhall, BS–Big Sky, OK–Okoruso, GH–Greenhorn, LB–Lubango.

128 and eolian sediments by the early Hesperian before being eroded through eolian processes
 129 (Malin and Edgett, 2000; Le Deit et al., 2013; Grant et al., 2014; Grotzinger et al., 2015). From
 130 orbit, the crater floor and lower strata of Aeolis Mons have spectral signatures consistent with
 131 alteration assemblages including hematite and phyllosilicates with variable hydrated sulfate and
 132 hydrated silica (Figure 1a; Fraeman et al., 2016). Higher up Aeolis Mons are strata with spectral
 133 signatures consistent with alteration assemblages dominated by monohydrated and polyhydrated
 134 sulfate minerals (a structure referred to as the “sulfate unit”). As of sol 2300, the most recent
 135 sampling date examined in this study, MSL had driven over 20 km laterally and gained 380 m of
 136 elevation but had not yet reached the mineral transition (Figure 1a). The three major stratigraphic
 137 units observed along the traverse and covered in this study are the Bradbury, Mount Sharp, and
 138 Siccar Point groups (Figure 1b).

139 The Bradbury group rocks make up part of the crater floor deposits (Grotzinger et al.,
 140 2015), and three Bradbury group drill samples were examined by CheMin: two lacustrine
 141 mudstones in the Yellowknife Bay formation, John Klein (JK) and Cumberland (CB) (see Figure
 142 1a for sampling locations and name abbreviations used throughout the text), and one fine-grained
 143 sandstone consisting of reworked deltaic and eolian sediments located in the Kimberley
 144 formation, Windjana (WJ) (Rice et al., 2017; Vaniman et al., 2014; Treiman et al., 2016;
 145 Morrison et al., 2018). Both mudstone samples were found to have crystalline Ca-sulfates
 146 (anhydrite and bassanite) and were initially modeled with 1 wt% pyrrhotite, though subsequent
 147 analyses were not able to model pyrrhotite with confidence for either sample (e.g., Morrison et

148 al., 2018; Rampe et al., 2020a). Models of XRD data showed that the sandstone sample
149 contained crystalline Ca-sulfates (anhydrite and bassanite), and the X-ray amorphous component
150 was notably high in SO₃ and Cl (Treiman et al., 2016; Dehouck et al., 2017). Ca-sulfates are
151 either completely or mostly associated with diagenetic features (e.g, veins, nodules, etc.;
152 Vaniman et al., 2014; Nachon et al., 2014, 2017).

153 As of sol 2300, CheMin had analyzed 12 drill hole locations within the Mount Sharp
154 group, which consists of mostly fluviolacustrine mudstones and fine-grained sandstones (e.g.,
155 Rivera-Hernández et al., 2020; Morris et al., 2016; Rampe et al., 2017, 2020b; Achilles et al.,
156 2020). Most of these rocks have geochemical compositions distinct from sediments in the
157 Bradbury group (Berger et al., 2020; Thompson et al., 2020), indicating a change in dominant
158 sediment sources (Bedford et al., 2019) and degree of chemical alteration (e.g., Mangold et al.,
159 2019; Hurowitz et al., 2017; Thorpe et al., 2021). The Mount Sharp group includes three targets
160 on Vera Rubin ridge (VRR; between ~ -4190 and -4140 m), a topographic ridge that shows
161 strong spectral signatures of hematite from orbit and from the ground, and is interpreted to have
162 experienced substantial diagenetic alteration relative to the surrounding units (e.g., Fraeman et
163 al., 2020; David et al., 2020; Horgan et al., 2020; L'Haridon et al., 2020; Rampe et al., 2020b).
164 The first three drill samples in the Mount Sharp group, Confidence Hills (CH), Mojave2 (MJ2),
165 and Telegraph Peak (TP) notably lacked crystalline Ca-sulfates, though Mojave2 did contain
166 lenticular features interpreted as pseudomorphs after gypsum (Kah et al., 2018), and instead were
167 found to contain jarosite (~1 wt% in CH, ~3 wt% in MJ2, and ~2 wt% in TP) (Rampe et al.,
168 2017). Ca-sulfates reappeared in the Buckskin sample (~1 wt% anhydrite) but jarosite was absent
169 (Rampe et al., 2017). Anhydrite was observed in all subsequent Mount Sharp group rocks
170 through VRR with some locations also bearing gypsum and/or bassanite, as well as jarosite
171 (Marimba, Quela, Sebina, Stoer, and Rock Hall) (Achilles et al., 2020; Rampe et al., 2020b).

172 The youngest strata considered in this study are the lithified eolian dunes comprising the
173 Siccar Point group, which unconformably lie on top of some sections of the Mount Sharp group
174 (Watkins et al., 2016; Banham et al., 2018). CheMin analyzed four drill samples within the
175 Siccar Point group prior to sol 2300: two within parent bedrock, Big Sky (BS) and Okoruso
176 (OK); and two within light-toned alteration “halos” surrounding central fractures, Greenhorn
177 (GH) and Lubango (LB) (Yen et al., 2017). The fracture-associated alteration halos are silica-
178 enriched zones ~50 cm wide that crosscut both the Mount Sharp and overlying Siccar Point
179 group rocks (Frydenvang et al., 2017; Yen et al., 2017). These alteration halos have been
180 interpreted as late diagenetic features that represent either chemical precipitates (Frydenvang et
181 al., 2017) or leaching residue (Yen et al., 2017) and may have formed through multiple fluid
182 episodes (Yen et al., 2017; Hausrath et al., 2018). The parent rocks were found to contain minor
183 crystalline Ca-sulfates (anhydrite and bassanite) and the alteration halos had significant
184 crystalline Ca-sulfates (anhydrite, bassanite, and gypsum) (Yen et al., 2017).

185 Multiple diagenetic events are recorded in the sedimentary rocks in Gale crater, but the
186 timeframes for these processes are somewhat poorly constrained. Buried sediments underwent
187 the diagenetic process of lithification, which includes porosity reduction through compaction and
188 cementation (Worden and Burley, 2003). The cementing agents for Gale crater rocks are not well
189 understood but likely consist of variable mixtures of syn-depositional to early diagenetic
190 crystalline Fe oxides (magnetite and hematite; Blaney et al., 2014; Bristow et al., 2015; Hausrath
191 et al., 2018; Tosca et al., 2018) and phyllosilicates (Bristow et al., 2015, 2018; Bridges et al.,
192 2015), X-ray amorphous Fe oxides and silicates (Smith et al., 2021), and Ca-sulfate (e.g., Blaney

193 et al., 2014; Newsom et al., 2016; Rapin et al., 2019), with potential Mg-sulfate cemented layers
194 in one ~10 m interval (Rapin et al., 2019).

195 The sedimentary rocks also contain evidence for diverse diagenetic processes spanning a
196 range of timeframes. Early diagenetic features include lenticular crystal pseudomorphs after
197 gypsum (likely deposited syndepositionally) in the Pahrump Hills section of the Mount Sharp
198 group (Kah et al., 2018) and desiccation cracks in the Sutton Island member of the Mount Sharp
199 group (Stein et al., 2018). Sections of the Sheepbed mudstone in the Bradbury group display
200 syneresis cracks filled with cement (fracture-filling raised ridges) likely comprised of Mg-rich,
201 Al-deficient smectitic clays, akageneite, and magnetite (McLennan et al., 2014; Siebach et al.,
202 2014; Léveillé et al., 2014). Features more pervasive along the rover traverse include concretions
203 and relief enhanced features that are sometimes associated with Mg- and Ca-sulfate (Stack et al.,
204 2014; VanBommel et al., 2016; Nachon et al., 2017; Sun et al., 2019), with one ChemCam point
205 on a nodular feature being consistent with jarosite (Nachon et al., 2017). Both the fracture-filled
206 raised ridges and concretions likely formed after the rocks were at least partially lithified but
207 before the formation of the light-toned veins that often cross-cut these features.

208 Extensive networks of light-toned veins and fracture-associated alteration halos suggest
209 that diagenetic fluids continued to circulate through the rocks for some time after lithification
210 (e.g., Nachon et al., 2014, 2017; Frydenvang et al., 2017; Yen et al., 2017; Gabriel et al., 2019;
211 Kronyak et al., 2019). The APXS and ChemCam instruments have been used to determine the
212 compositions of millimeter- to centimeter-scale light-toned veins and demonstrate that these
213 features are most often Ca-sulfates (Nachon et al., 2014, 2017; VanBommel et al., 2017;
214 Kronyak et al., 2019). APXS measurements show that the ~50 cm wide fracture-associated
215 alteration halos are relatively enriched in SiO₂ and SO₃ compared to the surrounding bedrock,
216 and CheMin analyses indicate these elements are mostly present as high fractions of amorphous
217 silica and sulfates and crystalline Ca-sulfates (Yen et al., 2017). The best constraint on the timing
218 of post-sedimentation fluid interactions is a K-Ar age date < 3 Ga (possibly as young as ~2.1 Ga)
219 for diagenetic jarosite in a single drill hole location (MJ2), indicating that diagenesis continued
220 for a significant amount of time after sedimentation ceased (Martin et al., 2017).

221

222 2.2 Sulfur-bearing Phase Detection with MSL Instrumentation

223 CheMin, APXS, and SAM are three of the main instruments onboard MSL capable of
224 detecting and differentiating between sulfur-bearing phases; each has different abundance and
225 phase detection limits. CheMin can detect most crystalline sulfur-bearing phases expected for
226 Gale crater if they are present in abundances > ~1 wt% (Blake et al., 2012). Any crystalline
227 sulfur-bearing phase present below that amount would be automatically allocated to the X-ray
228 amorphous composition, largely because at this abundance, phases lack prominent peaks in the
229 XRD patterns.

230 APXS measures elemental abundances and can detect SO₃ present in abundances > 0.2
231 wt%, as well as elements commonly associated with sulfur, such as Ca, Fe, and Mg present at
232 abundances > 0.2, 0.03, and 1 wt%, respectively (Gellert et al., 2015). S-bearing phases can be
233 inferred from correlations between sulfur and cations (e.g., McLennan et al., 2014; VanBommel
234 et al., 2016; Berger et al., 2020). APXS is assumed to measure SO₃ associated with both
235 crystalline and X-ray amorphous sulfur-bearing phases.

236 SAM has sensitivity for SO₂ at the ppm scale (Mahaffy et al., 2012), and there are no
237 known constraints on the degree of crystallinity of materials that are detectable by SAM (e.g.,
238 McAdam et al., 2014). SO₂ gas is evolved from volatile-bearing phases (e.g., minerals and
239 organic molecules) at characteristic temperatures, and so detectability is mostly driven by
240 whether or not a phase decomposes within the temperature range at which the SAM instrument
241 operates (ambient to 900°C; Mahaffy et al., 2012). Phases known to evolve SO₂ in the
242 temperature ranges examined by SAM include elemental sulfur and sulfonic acids, Fe-sulfates
243 and sulfides, Mg-sulfates, and Ca sulfites (Franz et al., 2017). Fe and Mg sulfites have not yet
244 been investigated in SAM-like conditions, but it is likely that they also decompose in the SAM
245 temperature range. Elemental sulfur, sulfonic acids, and Fe sulfides that are oxidized during
246 pyrolysis decompose at temperatures between ~125 and 400°C, Fe-sulfates and sulfides
247 generally decompose at temperatures between ~400 and 700°C, Mg-sulfates decompose at
248 temperatures between ~700 and 900°C, and Ca sulfites decompose at temperatures between ~750
249 and 850°C (McAdam et al., 2014; Franz et al., 2017; Sutter et al., 2017). Ca-sulfates mostly
250 decompose at temperatures beyond the upper temperature limit for SAM and thus cannot be
251 detected by SAM (e.g., Mu and Perlmutter, 1981; McAdam et al., 2014). However, some phases
252 expected for the Martian surface, such as Ca-, Mg-, and Fe-perchlorates, can catalyze the
253 decomposition of crystalline Ca-sulfates so that Ca-sulfates could have SO₂ peak initiation
254 temperatures ~600°C in the temperature range of SAM; However, the catalyzed Ca-sulfates do
255 not fully decompose within SAM's temperature range (e.g, McAdam et al., 2016).

256 Few studies have examined EGA SO₂ traces for amorphous, poorly crystalline, and/or
257 nanocrystalline sulfates. McAdam et al. (2014) showed that amorphous ferric sulfate has an EGA
258 SO₂ trace nearly identical to that of crystalline ferric sulfate. Though they did not study sulfates,
259 Archer et al. (2013) showed that a reduction in particle size for calcite lowered the peak
260 decomposition temperature by ~200°C (Archer et al., 2013). These studies suggest that
261 amorphous, poorly crystalline, and/or nanocrystalline sulfates may evolve SO₂ at temperatures
262 approximately equal to or lower than (up to ~200°C lower) those of μm to mm sized particles.
263 Therefore, if present in Gale crater rocks, amorphous, poorly crystalline, and nanocrystalline Ca-
264 sulfates would still likely evolve SO₂ outside the range measured by SAM, while amorphous,
265 poorly crystalline, and nanocrystalline Mg and Fe-sulfates should be detectable. It is not known
266 if catalysts will also reduce Ca-sulfate's SO₂ peak initiation temperature if the Ca-sulfate is
267 amorphous.

268 269 **3 Methods:**

270 3.1. Mass Balance Approach

271 This study uses the results of Smith et al. (2021), who calculated bulk X-ray amorphous
272 component compositions for all rock samples through Vera Rubin ridge (VRR; up to sol 2300)
273 and reported X-ray amorphous FeO_T and SiO₂ contents. The methods from that study are
274 summarized here.

275 Bulk X-ray amorphous component compositions are estimated through mass balance
276 models. First, XRD-derived minerals and abundances from CheMin are converted to a bulk
277 crystalline component composition. Then, assuming APXS measurements of drill samples
278 represent the bulk sample geochemistry (crystalline + X-ray amorphous), the crystalline
279 component composition is subtracted from the bulk composition, and the residual represents the
280 bulk X-ray amorphous component composition, with the uncertainties listed below. Since APXS

281 frequently acquires multiple compositions of drill samples (e.g., undisturbed rock, drill tailings,
282 discard pile), Smith et al. (2021) used the same APXS measurements from previous calculations,
283 where applicable, and otherwise averaged compositions from multiple APXS measurements
284 (Table DR3). It should be noted that recommended APXS composition results for the drill sites
285 covered in this study are presented in Berger et al. (2020), published after the calculations were
286 performed for Smith et al. (2021), and in some cases the recommended compositions are
287 different from those used by Smith et al. (2021) (Table DR3). Mineral abundances and
288 compositions were from the published literature (Morrison et al, 2018; Achilles et al., 2020;
289 Rampe et al., 2020b) and are summarized in the Supplemental Material for Smith et al. (2021).

290 Uncertainties in bulk X-ray amorphous component compositions result from the
291 following caveats and assumptions made for these calculations, discussed in detail in Dehouck et
292 al. (2014) unless otherwise noted: (1) compositions of crystalline phases that might be present
293 below the detection limit of CheMin XRD (~1 wt%) are allocated to the X-ray amorphous
294 component composition by default; (2) minor elemental substitutions in crystalline minerals
295 (e.g., Ti, Mn, Cr, P) not detectable by XRD are also allocated to the X-ray amorphous
296 component composition; (3) when present, poorly constrained clay mineral compositions make it
297 difficult to precisely determine the X-ray amorphous component composition; for samples with
298 ~25 wt% phyllosilicates in the crystalline component, different plausible clay compositions
299 result in differences of \leq ~2 wt% CaO, MgO, and FeO_T in the X-ray amorphous components
300 (Dehouck et al., 2014); (4) uncertainties in CheMin-derived mineral abundances from standard
301 errors and differences in fitting efforts (Morrison et al., 2018; see also Supplemental Material)
302 create a range of possible crystalline component compositions, which results in a range of
303 possible X-ray amorphous component compositions; Smith et al. (2021) calculated a “best
304 estimate” composition for each X-ray amorphous component using the reported mineral
305 abundances from CheMin (i.e., did not consider mineral uncertainties) as well as a range of X-
306 ray amorphous component compositions using the mineral abundance uncertainties. The
307 minimum and maximum X-ray amorphous SO₃ contents for each sample varied on average by
308 21% of the reported “best estimate” value (Table DR2); (5) the general accuracy of quantitative
309 XRD analytical results for multiphase mixtures is dependent on a great number of factors (e.g.,
310 modeling method, background models, accuracy of phase identification, etc.) and is a continuous
311 area of research with a complicated discussion that is beyond the scope of this paper. We
312 mention this here even though the error cannot be quantified, and note that for a given Mars
313 analog sample, both methods employed by the CheMin team (Rietveld refinement and
314 FULLPAT) produce similar mineralogy results, and therefore similar X-ray amorphous
315 component compositions for Mars analog samples (Smith et al., 2018); (6) there are uncertainties
316 on the oxide abundances from APXS measurements detailed in Gellert and Clark (2015) with a
317 relative uncertainty of 15% for SO₃ (see Table DR3 for the errors on each oxide abundance); (7)
318 the new Feed-Extended Drilling/Feed-Extended Sample Transfer (FED/FEST) drilling technique
319 does not allow drill fines to be homogenized in the Collection and Handling for In-Situ Martian
320 Rock Analysis (CHIMRA) device before delivery to CheMin (Rampe et al., 2020a), which
321 complicates the assumption that CheMin and APXS measure the same sample. The first dill site
322 after the anomaly was Duluth (DU) and so this uncertainty is mostly an issue for samples from
323 Duluth (DU) on. Some of these sources of uncertainty can be quantified and we propagate errors
324 to give a minimum error on X-ray amorphous component compositions (calculations described
325 in the Supplemental Text).

326 3.2. SAM Evolved SO₂ trace analyses

327 To investigate the X-ray amorphous S-bearing phase compositions determined from the
328 mass balance calculations, we report SAM SO₂ evolved gas analysis (EGA) results for five of the
329 nineteen samples in this study (CH, BS1, GH1, MJ2, and WJ; SAM sometimes measures a
330 sample more than once and so the numbers indicate the subsample; Sutter et al., 2017). These
331 five samples were primarily selected because they have relatively high X-ray amorphous SO₃
332 contents based on the mass balance calculation results. Two of the samples were selected to
333 examine potential differences between X-ray amorphous sulfur compositions in parent Siccar
334 Point rocks (BS) and alteration halos (GH) formed through late-stage diagenetic fluid alteration.
335 The other three samples were selected because the peak fitting methods described below
336 provided results with relatively low uncertainties. Thus, these samples may not be representative
337 of the full suite of X-ray amorphous sulfur-bearing materials compositions at Gale crater.

338 Volatile content for each sample was determined through pyrolysis of drill fines using the
339 SAM instrument, which consists of a quadrupole mass spectrometer (QMS), gas chromatograph
340 (GC), and tunable laser spectrometer (TLS) (Mahaffy et al., 2012). Samples were heated from
341 ~40°C to ~870 or 900°C (depending on the sample) at a rate of 35°C/min (Sutter et al., 2017;
342 McAdam et al., 2020). Evolved sample SO₂ gas was directly monitored by the QMS resulting in
343 signal versus temperature curves referred to as EGA traces. Evolved SO₂ gas totals were
344 combined with estimated sample mass deliveries to SAM to calculate evolved gas contents (e.g.,
345 wt %) (Sutter et al., 2017).

346 To resolve the S-bearing phases and their abundances from SAM data, peaks were fit to
347 the SO₂ EGA traces using the data analysis and graphing software Origin. Peaks were either fit
348 visually or by using the 2nd derivative technique to locate peaks that are difficult to see. Once the
349 peaks were identified, they were fit with Gaussian (for symmetric peaks) or BiGaussian (for
350 asymmetric peaks) curves. The peaks were assigned to phases (e.g., Mg-S, Fe-S) and the areas
351 under the peaks were used to determine the abundances of the phases in each sample. In four of
352 the five samples (CH, GH1, BS1, WJ), one modeled peak fell within the temperature ranges
353 shared by both Mg-S and Fe-S phases (~700°C) and so it could not be determined to which
354 phase the peaks should be attributed (Figure S1). For these samples, we calculated a range of
355 phase abundances, first by ignoring the contribution from the “Mg-S or Fe-S” peak altogether,
356 next by attributing the “Mg-S or Fe-S” peak solely to Mg-S phases, and last by attributing the
357 “Mg-S or Fe-S” peak solely to Fe-S phases.

358 3.3. “Difference method” (assumed X-ray amorphous Ca-sulfate quantification)

359 Assuming SAM can detect all S-bearing phases present in Gale crater except Ca-sulfates,
360 we attribute the difference between SO₃ contents measured by APXS and SAM (ΔSO_3) to Ca-
361 sulfate (Sutter et al., 2017) and calculate the abundance of amorphous Ca-sulfate for samples
362 with SAM data in the following steps:

- 363 1) $\Delta\text{SO}_3 = \text{SO}_3_{\text{APXS}} - \text{SO}_3_{\text{SAM}}$
364 2) $\text{SO}_3_{\text{amorph Ca-S}} = \Delta\text{SO}_3 - \text{SO}_3_{\text{cryst Ca-S}}$

365 Where $\text{SO}_3_{\text{APXS}}$ is the bulk SO₃ content (wt%) measured in each sample with the APXS
366 instrument, SO_3_{SAM} is the SO₃ content (wt%) measured in each sample with the SAM
367 instrument, $\text{SO}_3_{\text{amorph Ca-S}}$ is the abundance (wt%) of amorphous Ca-sulfate in each sample, and
368 $\text{SO}_3_{\text{cryst Ca-S}}$ is the wt% abundance of SO₃ associated with crystalline Ca-sulfates calculated from
369 CheMin-derived Ca-sulfate abundances. Thus, in the cases where crystalline Ca-sulfates could
370 not account for all the difference between APXS and SAM measurements ($\Delta\text{SO}_3 - \text{SO}_3_{\text{cryst Ca-S}} >$

371 0), the remaining SO₃ was attributed to amorphous Ca-sulfates. Uncertainties associated with this
372 assumption include the fact that SAM SO₃ abundances are relatively low (< 7 wt%) and can have
373 significant errors associated with the measurements (up to 3 wt%; Table DR5). Additionally, it is
374 possible that some of the difference between APXS and SAM SO₃ measurements could be
375 attributed to other phases with decomposition temperatures above the SAM range such as,
376 complexes involving SO₃ adsorbed onto X-ray amorphous alteration products (discussed in
377 greater detail below). Another assumption made in the calculation of the X-ray amorphous
378 material compositions is that APXS, CheMin, and SAM all measure the same material. This is
379 likely an acceptable assumption for the samples with detailed SAM analyses in this study, but is
380 possibly more problematic for sites sampled after the drilling anomaly since drill fines are not
381 homogenized before delivery to CheMin and SAM.

382

383 **4 Results:**

384 Figure 2a shows the bulk SO₃ in each rock allocated to the crystalline and X-ray
385 amorphous fractions based on APXS and CheMin data. On average, bulk rocks contain ~5.3
386 wt% crystalline SO₃ (standard deviation = 4.4 wt%; range = 0.7 – 14.1 wt%) and ~4.2 wt%
387 amorphous SO₃ (standard deviation = 2.6 wt%; range = ~0.2 – 9.9 wt%) (Table DR1). Thus,
388 between 20 and 90% of any sample's sulfur content is in the X-ray amorphous state. There is a
389 possible weak correlation between SO₃ in the crystalline state and SO₃ in the X-ray amorphous
390 state, with $r^2=0.25$ (Figure 2b).

391 A molar SO₃-MgO-CaO ternary diagram (Figure 3a) helps characterize potential
392 compositions of X-ray amorphous sulfur-bearing materials in each drill hole location. In this
393 diagram, the uppermost apex represents Fe-sulfate, as well as any sulfate composition other than
394 Ca or Mg-sulfates (e.g., Al sulfate, Na sulfate, K sulfate, adsorbed SO₃, etc.). For this diagram,
395 all sulfur is assumed to be oxidized, and if present, phases such as elemental sulfur and Fe
396 sulfides would plot at the uppermost apex. Any samples with X-ray amorphous compositions
397 that lie above the kieserite—gypsum tie line must have some contribution from those “other”
398 sulfates because they do not have enough amorphous MgO and CaO to balance the amorphous
399 SO₃. For these drill hole locations (RH, CH, BK, and MB), we can infer that their X-ray
400 amorphous components represent complex/variable mixtures of X-ray amorphous Ca, Mg, and
401 Fe + “other” sulfates, and possibly mixed cation sulfates. Any sample with an X-ray amorphous
402 component composition that plots below the kieserite—gypsum tie line has more amorphous
403 MgO and/or CaO than amorphous SO₃. For these drill hole locations (TP, DU, QL, SB, JK, WJ,
404 BS, ST, OU, HF, and CB), we can infer that their X-ray amorphous components represent
405 complex/variable mixtures of X-ray amorphous Ca, Mg, and Fe + “other” sulfates with other
406 amorphous and poorly crystalline Mg and Ca bearing phases (e.g., silicates). Samples with X-ray
407 amorphous compositions that fall on or close to the kieserite—gypsum tie line have amorphous

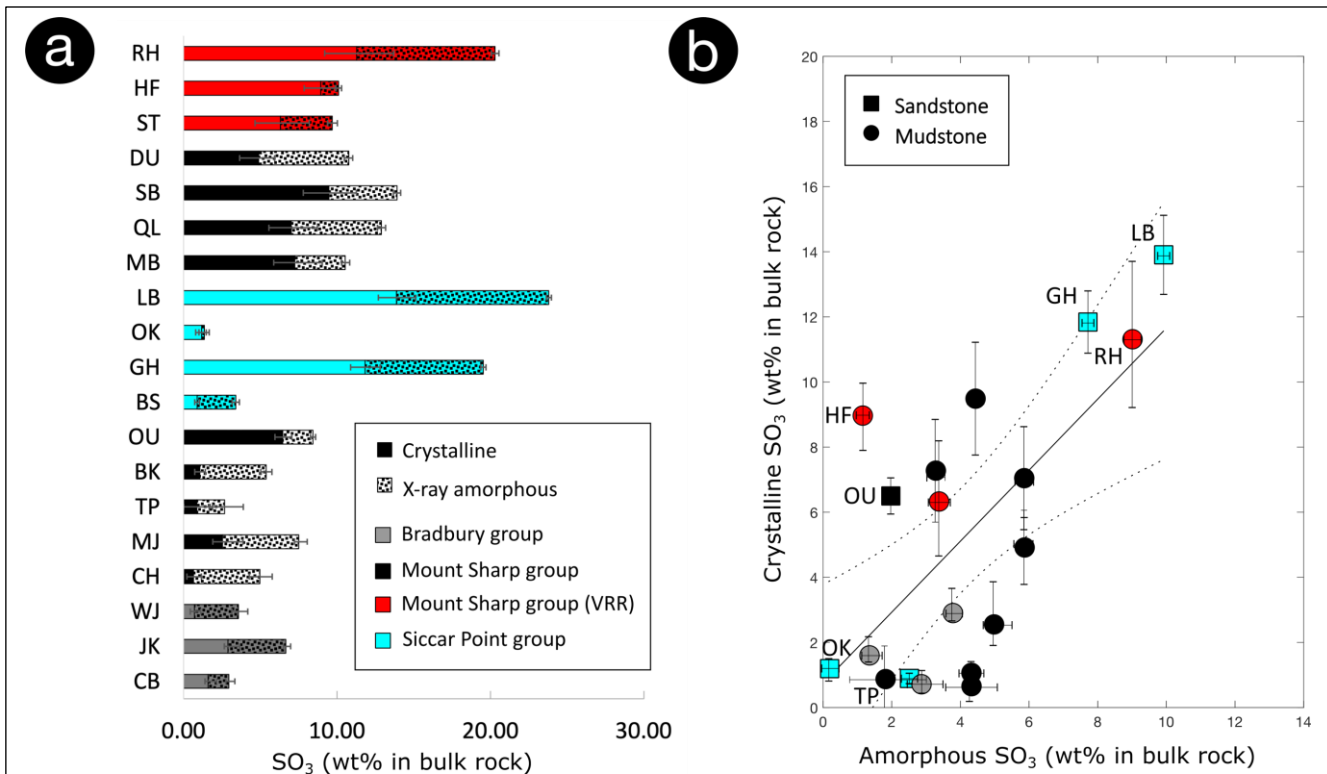


Figure 2. (a) Distribution of bulk SO₃ in the crystalline and X-ray amorphous state for each drill hole sample; bulk SO₃ is measured by the APXS instrument, crystalline SO₃ is measured by the CheMin instrument, and X-ray amorphous SO₃ is calculated using the mass balance method as described in the methods section. (b) Plot showing X-ray amorphous SO₃ from mass balance calculations vs. SO₃ in the crystalline component with some outliers labeled for reference; all contents given in wt% of bulk rock; solid black line is the linear fit to the data with $r^2 = 0.445$ (adjusted $r^2 = 0.412$) and dotted lines represent ± 2 -standard error. See Supplemental Materials for description of how error bars were calculated.

408 MgO and CaO that roughly balance the amorphous SO₃. For these locations (MJ, GH, and LB),
 409 it is possible that they contain mostly mixtures of Mg and Ca-sulfates (or mixed cation-Ca, Mg-
 410 sulfates) with essentially no Fe + “other” sulfates.

411 SAM SO₂ EGA trace analysis results are shown in Table 2 and peak fitting models are
 412 shown in Figure S1. All five samples examined in this study with SAM data show evolved SO₂
 413 trace analysis results that indicate some Mg-S. Using the abundance of SO₂ associated with Mg-
 414 S phases to calculate abundances of X-ray amorphous Mg-sulfates of kieserite composition, we
 415 find all five samples would have Mg-sulfates at or above the ~1 wt% detection limit of CheMin
 416 (average = 4.1 wt%; range = 1.0 – 5.6 wt%) (Table DR7) but CheMin did not detect any Mg-S
 417 phases (Table 1).

418 Likewise, all these samples measured by SAM contain some fraction of Fe-S phases.
 419 CheMin detected crystalline Fe-S phases in only two of the five samples (CH and MJ2; Table 1),
 420 and in both cases SAM analysis indicates that these samples contain more SO₃ related to Fe-S
 421 phases than the CheMin jarosite can account for. Assumptions of either a schwertmannite or
 422 melanterite composition for the leftover abundance of SAM-measured SO₂ associated with Fe-S

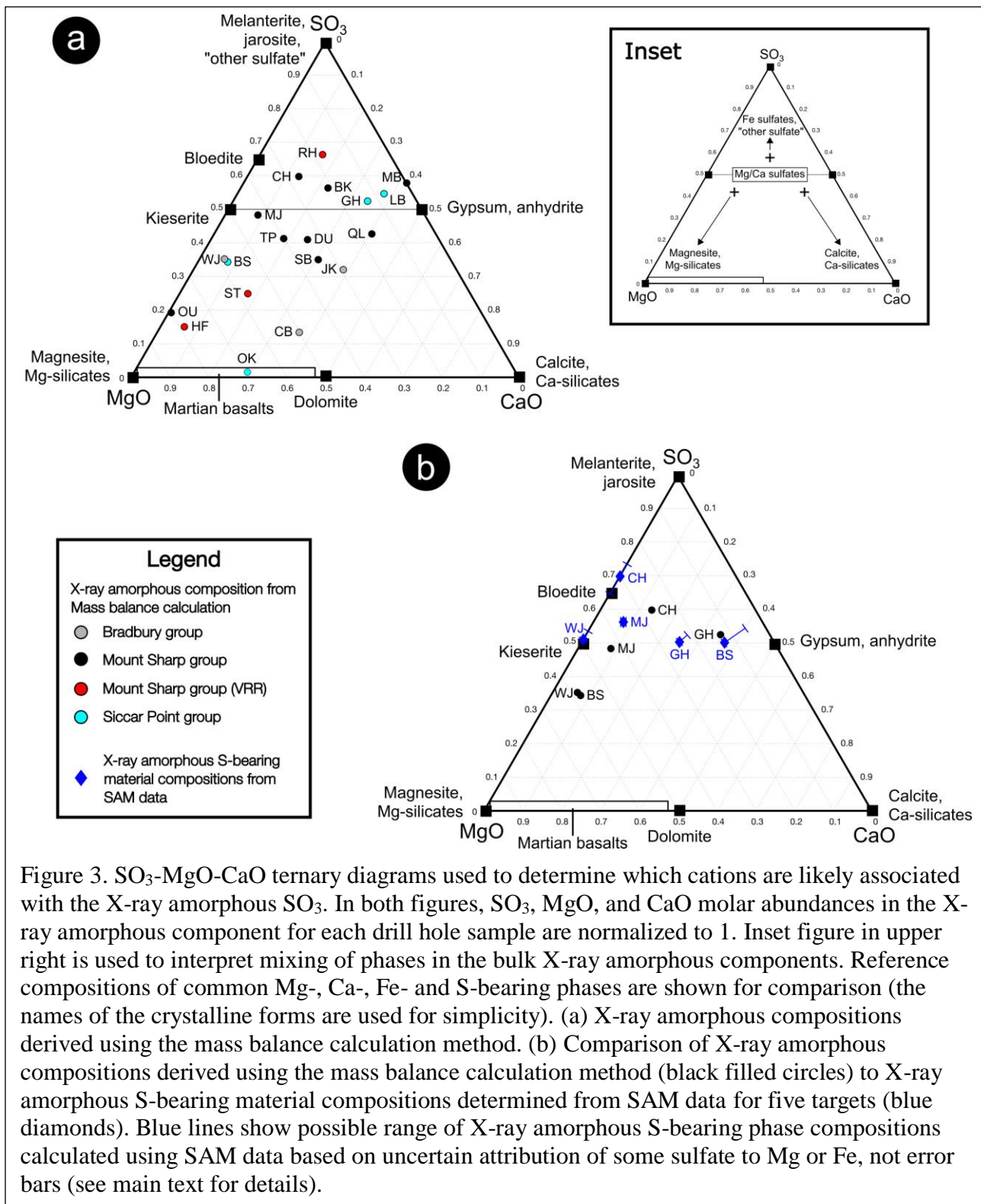


Figure 3. SO_3 -MgO-CaO ternary diagrams used to determine which cations are likely associated with the X-ray amorphous SO_3 . In both figures, SO_3 , MgO, and CaO molar abundances in the X-ray amorphous component for each drill hole sample are normalized to 1. Inset figure in upper right is used to interpret mixing of phases in the bulk X-ray amorphous components. Reference compositions of common Mg-, Ca-, Fe- and S-bearing phases are shown for comparison (the names of the crystalline forms are used for simplicity). (a) X-ray amorphous compositions derived using the mass balance calculation method. (b) Comparison of X-ray amorphous compositions derived using the mass balance calculation method (black filled circles) to X-ray amorphous S-bearing material compositions determined from SAM data for five targets (blue diamonds). Blue lines show possible range of X-ray amorphous S-bearing phase compositions calculated using SAM data based on uncertain attribution of some sulfate to Mg or Fe, not error bars (see main text for details).

423 phases produces Fe-sulfates (other than jarosite) at or above the ~1 wt% detection limit of
 424 CheMin for these samples (CH and MJ2) (Table DR7). In all samples except Confidence Hills
 425 (CH), SO_3 from X-ray amorphous Mg-S is more abundant than SO_3 from X-ray amorphous Fe-S,

426 even when the ambiguous “Fe-S or Mg-S” peaks are attributed to Fe-S phases (Table 2 and
 427 Table DR4).

428 Three of the five samples examined in this study with SAM data (MJ2, BS1 and GH1) do
 429 not have enough crystalline Ca-sulfates (“best estimate” abundances) to account for all the
 430 difference between APXS and SAM measurements ($\Delta\text{SO}_3 - \text{SO}_3_{\text{cryst Ca-S}} > 0$), and so the
 431 remaining SO_3 was attributed to amorphous Ca-sulfates. Assuming an anhydrite composition for
 432 the X-ray amorphous Ca-S phases, we find that these three samples would have Ca-sulfates
 433 (other than those already detected) at or above the ~1 wt% detection limit of CheMin (average =
 434 3.2 wt%; range = 1.2 – 5.5 wt%) (Table DR7). Even when the maximum possible Ca-sulfate
 435 abundances are taken into account (“best estimate” abundance + 2-sigma uncertainty for each
 436 crystalline Ca-sulfate phase), these three samples do not have enough crystalline Ca-sulfates to

Table 1. Crystalline sulfur-bearing phases in Gale crater rocks as determined by CheMin analysis.

Sample	CheMin mineralogy				Calculated from CheMin mineralogy	
	Jarosite	Bassanite	Anhydrite	Gypsum	SO ₃ (wt%) in crystalline Fe-sulfate	SO ₃ (wt%) in crystalline Ca-sulfate
CB	0.0 (0.0)	1.3 (0.1)	0.7 (0.4)	0.0 (0.0)	0.00	1.21
JK	0.0 (0.0)	1.4 (0.1)	2.1 (0.4)	0.0 (0.0)	0.00	2.03
WJ	0.0 (0.0)	0.5 (0.2)	0.5 (0.3)	0.0 (0.0)	0.00	0.58
CH	1.1 (0.7)	0.0 (0.0)	0.0 (0.0)	0.0 (0.0)	0.40	0.00
MJ	3.2 (0.7)	0.0 (0.0)	0.0 (0.0)	0.0 (0.0)	1.14	0.00
TP	1.8 (2.1)	0.0 (0.0)	0.0 (0.0)	0.0 (0.0)	0.63	0.00
BK	0.0 (0.0)	0.0 (0.0)	0.8 (0.2)	0.0 (0.0)	0.00	0.47
OU	0.0 (0.0)	0.0 (0.0)	3.2 (0.6)	2.9 (0.2)	0.00	3.56
MB	0.3 (0.6)	0.8 (1.0)	2.3 (1.4)	1.3 (0.9)	0.12	2.59
QL	0.5 (0.6)	1.9 (0.9)	3.1 (0.7)	0.4 (0.7)	0.18	3.19
SB	0.9 (0.6)	1.1 (0.6)	5.2 (1.6)	1.1 (1.1)	0.32	4.34
DU	0.0 (0.0)	3.3 (0.3)	1.5 (0.5)	0.2 (0.2)	0.00	2.90
ST	1.1 (0.3)	0.5 (0.2)	3.3 (0.3)	2.5 (0.8)	0.39	3.72
HF	0.0 (0.0)	1.2 (0.3)	3.8 (0.5)	2.4 (0.5)	0.00	4.33
RH	2.0 (0.1)	0.0 (0.0)	10.1 (1.5)	0.0 (0.0)	0.72	5.92
BS	0.0 (0.0)	0.0 (0.0)	1.2 (0.2)	0.0 (0.0)	0.00	0.71
GH	0.0 (0.0)	1.4 (0.5)	5.6 (0.5)	0.0 (0.0)	0.00	4.14
OK	0.0 (0.0)	0.8 (0.3)	0.5 (0.3)	0.0 (0.0)	0.00	0.77
LB	0.0 (0.0)	2.4 (0.5)	3.3 (0.5)	0.6 (0.4)	0.00	3.75

Note: all values are wt% in total sample (crystalline + phyllosilicates + X-ray amorphous) and values in parentheses are 2-sigma uncertainties on mineral abundances in %. See Figure 1 caption for full sample name abbreviated here.

Table 2. SAM SO₂ EGA trace peak fitting results.

Peak #	Fit	Area (%)	Likely phase	Fe-S ^a	Mg-S ^a
Windjana					
1	Gaussian	2.4 (1.9)	Fe-S		
2	Gaussian	9.3 (0.7)	Fe-S or Mg-S		
3	Gaussian	12.2 (2.7)	Mg-S	0.0	1.0
4	Gaussian	68.7 (6.3)	Mg-S		
5	Bi-Gaussian	7.4 (2.4)	Mg-S		
Confidence Hills					
1	Bigaussian	27.9 (0.9)	Fe-S		
2	Gaussian	18.2 (4.9)	Fe-S		
3	Gaussian	18.7 (1.0)	Fe-S or Mg-S	0.6	0.4
4	Gaussian	27.7 (5.4)	Mg-S		
5	Gaussian	7.5 (1.9)	Mg-S		
Mojave2					
1	Bi-Gaussian	20.3 (2.2)	Fe-S		
2	Bi-Gaussian	4.9 (3.5)	Fe-S		
3	Bi-Gaussian	19.2 (4.3)	Mg-S		
4	Gaussian	12.3 (0.5)	Mg-S	0.3	0.7
5	Gaussian	32.6 (6.7)	Mg-S		
6	Gaussian	4.9 (3.1)	Mg-S		
7	Bi-Gaussian	5.8 (0.9)	Mg-S		
Big Sky (1)					
1	Bigaussian	1.9 (1.3)	Fe-S		
2	Bigaussian	56.7 (3.9)	Fe-S or Mg-S		
3	Bigaussian	11.5 (7.1)	Mg-S	0.0	1.0
4	Bigaussian	25.4 (3.2)	Mg-S		
5	Bigaussian	4.5 (0.8)	Mg-S		
Greenhorn (1)					
1	Gaussian	4.0 (1.2)	Fe-S		
2	Gaussian	13.7 (2.4)	Fe-S or Mg-S		
3	Gaussian	6.5 (0.4)	Mg-S		
4	Gaussian	48.0 (2.4)	Mg-S	0.0	1.0
5	Gaussian	7.0 (2.4)	Mg-S		
6	Bigaussian	20.9 (1.5)	Mg-S		

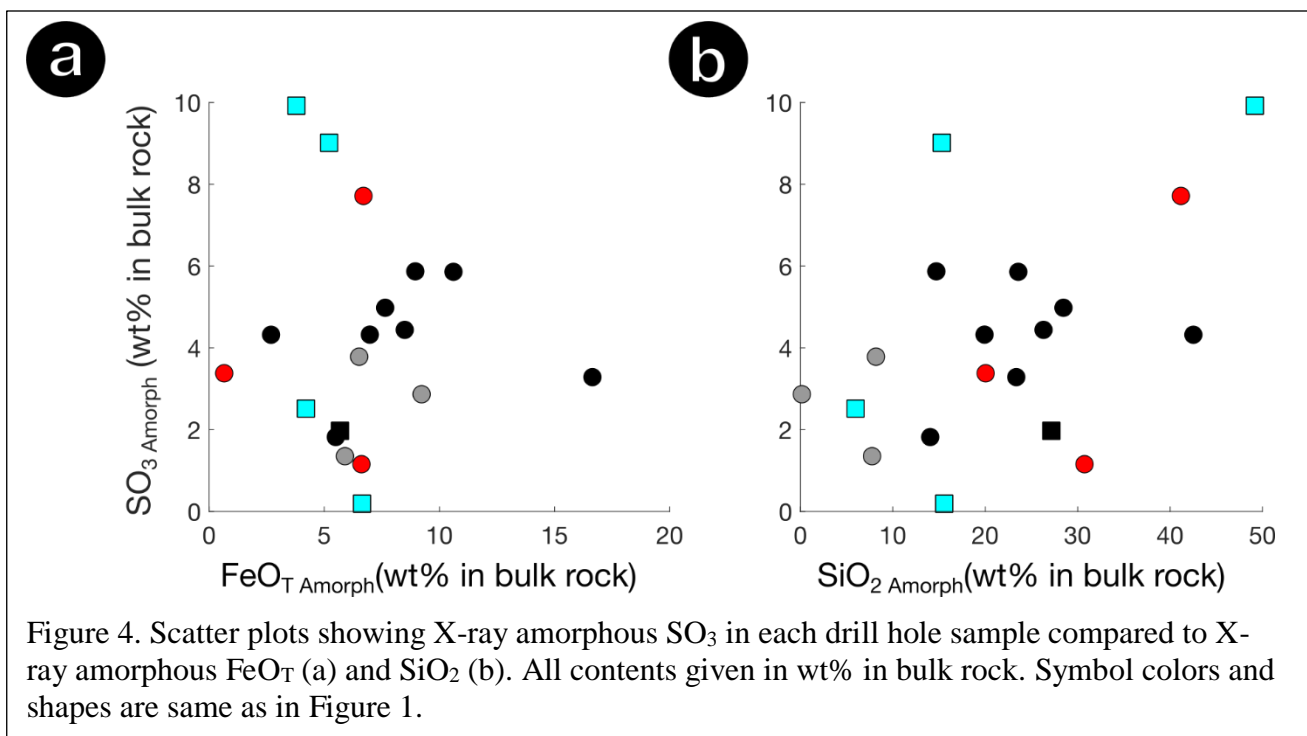
^aFraction of phase calculated by ignoring ambiguous peaks. See text in Supplemental for details.

437 account for all the difference between APXS and SAM measurements ($\Delta\text{SO}_3 - \text{SO}_3_{\text{cryst Ca-S}} > 0$)
438 and the maximum crystalline Ca-sulfate abundances only minimally change the resulting
439 abundances of X-ray amorphous Ca-sulfates (average = 2.8 wt%; range = 1.2 – 4.7 wt%).
440 Additionally, mass balance calculations indicate that these three samples have more moles of X-
441 ray amorphous CaO than moles of SO₃ assumed to be associated with X-ray amorphous Ca-S
442 phases. In other words, assuming a 1:1 molar ratio of SO₃:CaO, there is always excess X-ray
443 amorphous CaO, implying that the assumed Ca-S associated SO₃ is reasonable and that there are
444 other Ca-bearing X-ray amorphous phases present in these samples.

445 SAM-derived X-ray amorphous S-bearing compositional ranges were plotted on the same
446 ternary diagram as the mass balance calculation results to determine how well these two

447 techniques agree (Figure 3b). Ternary plot compositions were calculated for SAM data by
 448 combining SAM Mg-S and Fe-S (with crystalline Fe-S phases subtracted) peak integration
 449 results with X-ray amorphous Ca-sulfate abundances calculated through equations 1 and 2 (see
 450 Supplemental Material for detailed calculation methods). Samples that had relatively large
 451 ambiguous “Fe-S or Mg-S” peaks (e.g., BS1) have relatively large compositional ranges that are
 452 illustrated by longer blue lines (Figure 3b; blue diamonds show the case where the ambiguous
 453 peaks are ignored). Overall, agreement between the mass balance and SAM-derived X-ray
 454 amorphous component compositions seems to depend on the X-ray amorphous SO₃ contents. For
 455 the samples with relatively high X-ray amorphous SO₃ contents (CH, MJ2 and GH), the X-ray
 456 amorphous S-bearing phase compositional ranges calculated using SAM data show reasonable
 457 agreement to the X-ray amorphous compositions calculated using the mass balance method.
 458 These results indicate that, for these three samples, CaO and MgO in the X-ray amorphous
 459 components are likely associated with S-bearing materials (as opposed to silicates, for example).
 460 For the samples with relatively low X-ray amorphous SO₃ contents (BS and WJ), there are
 461 relatively large differences between the mass balance and SAM-derived compositions, indicating
 462 that the X-ray amorphous components for these samples also likely contain significant MgO-
 463 bearing phases (e.g., silicates). Because it is difficult to separate cation associations with sulfur
 464 vs. other materials such as silicates, we urge significant caution when using mass balance
 465 calculation results to infer amorphous sulfate compositions, and recommend performing detailed
 466 SAM SO₂ trace analyses.

467 Even for samples with relatively high X-ray amorphous SO₃ contents, there are some
 468 discrepancies between the compositions of X-ray amorphous sulfates in each sample based on
 469 SAM and mass balance calculation results. For example, the Greenhorn (GH) and Confidence
 470 Hills (CH) samples have more Mg-rich SAM-derived X-ray amorphous sulfur-bearing phase
 471 compositions, while the mass balance calculation results would indicate that the X-ray
 472 amorphous sulfur-bearing phases are more Ca-sulfate-rich (Figure 3b). It is possible that some of



473 the SAM-derived SO₂ attributed to Mg-S phases could, in part, come from the catalyzed
474 decomposition of crystalline or amorphous Ca-sulfates. Indeed, these two samples show
475 particularly high-temperature peaks in the evolved SO₂ release traces that are consistent with
476 catalyzed Mg-sulfate and Ca-sulfate phases (Franz et al., 2017). However, they also have
477 relatively low to moderate abundances of evolved O₂ attributed to perchlorate (a possible
478 catalyst) when compared to other samples (Sutter et al., 2017). Perhaps in addition to small
479 amounts of catalyzed Ca-sulfates, this discrepancy could also result from uncertainties in the
480 bulk X-ray amorphous component compositions due to uncertainties in mineral compositions
481 and abundances.

482 Overall, both the mass balance compositions and the SAM data indicate that the X-ray
483 amorphous S-bearing material in most Gale crater rocks likely consists of complex/variable
484 mixtures of Mg-S, Fe-S, and possibly Ca-S phases. There is no strong trend in X-ray amorphous
485 S-bearing material composition with stratigraphic group (Figure 3a). However, the Siccar Point
486 samples with detectable X-ray amorphous S-bearing materials (BS, GH, and LB) have a
487 significant fraction of the X-ray amorphous S-bearing material attributed to Ca-S phases whereas
488 most of the non-VRR Mount Sharp group rocks (except OU) have X-ray amorphous components
489 that roughly cluster around the tie line between Mg-S and Ca-S phases.

490 Calculated X-ray amorphous SO₃
 491 contents are compared to the other two most
 492 abundant oxides in the X-ray amorphous
 493 components, SiO₂ and FeO_T, in Figure 4. X-ray
 494 amorphous SO₃ shows no correlation with X-
 495 ray amorphous FeO_T content (Figure 4a), and
 496 there exists a possible weak positive correlation
 497 with X-ray amorphous SiO₂ (r² value = 0.235;
 498 Figure 4b).

499 Figure 5 shows stratigraphic variations
 500 in SO₃ (wt%) in the X-ray amorphous
 501 component for each drill hole location. Each
 502 stratigraphic group contains a range of X-ray
 503 amorphous SO₃ contents, and there is no
 504 systematic change in X-ray amorphous SO₃
 505 contents between stratigraphic groups that
 506 otherwise show geochemical evidence for
 507 changes in sediment source (e.g., across the
 508 Bradbury - Mount Sharp group boundary). The
 509 Siccar Point group location Okoruso (OK) has
 510 the lowest bulk SO₃ and is the only location to
 511 have almost no X-ray amorphous SO₃ (Table
 512 DR2). The locations with the greatest X-ray
 513 amorphous SO₃ contents are found in the Siccar
 514 Point group alteration halos Greenhorn and
 515 Lubango (GH and LB) and in the VRR sample
 516 Rock Hall (RH).

517 5 Discussion:

518 5.1 Constraining X-ray amorphous 519 sulfur-bearing phases 520

521 No single instrument on the rover can distinguish with certainty the nature of the X-ray
 522 amorphous sulfur-bearing phases. However, we can combine observations to put some
 523 constraints on these phases. All locations examined in this study except Okoruso (OK) have X-
 524 ray amorphous SO₃ contents > 1 wt%, and both mass balance calculation and SAM analysis
 525 results indicate that the X-ray amorphous SO₃ represents mixtures of Mg-S and Fe-S phases,
 526 with likely contributions from Ca-S phases. Other possible contributors include reduced phases,
 527 e.g., sulfides or sulfur in glass, that were oxidized during the SAM measurements (McAdam et
 528 al., 2014; Sutter et al., 2017), and sulfate anions adsorbed onto X-ray amorphous alteration
 529 products (e.g., Rampe et al., 2016). The ratios of these phases likely vary between sampling
 530 locations, which is reflected in the varying ratios of Mg-S, Fe-S, and Ca-S phases.

531 SAM EGA SO₂ traces and sulfur isotope data can be used to indicate the oxidation state
 532 of sulfur in sulfur-bearing phases. For most of the samples covered in this study (CB through
 533 BS/GH), previous SAM analyses show a wide range of sulfur isotopic compositions (Franz et al.,
 534 2017). Two of the samples (CB and OU) have significantly ³⁴S-depleted isotopic compositions,

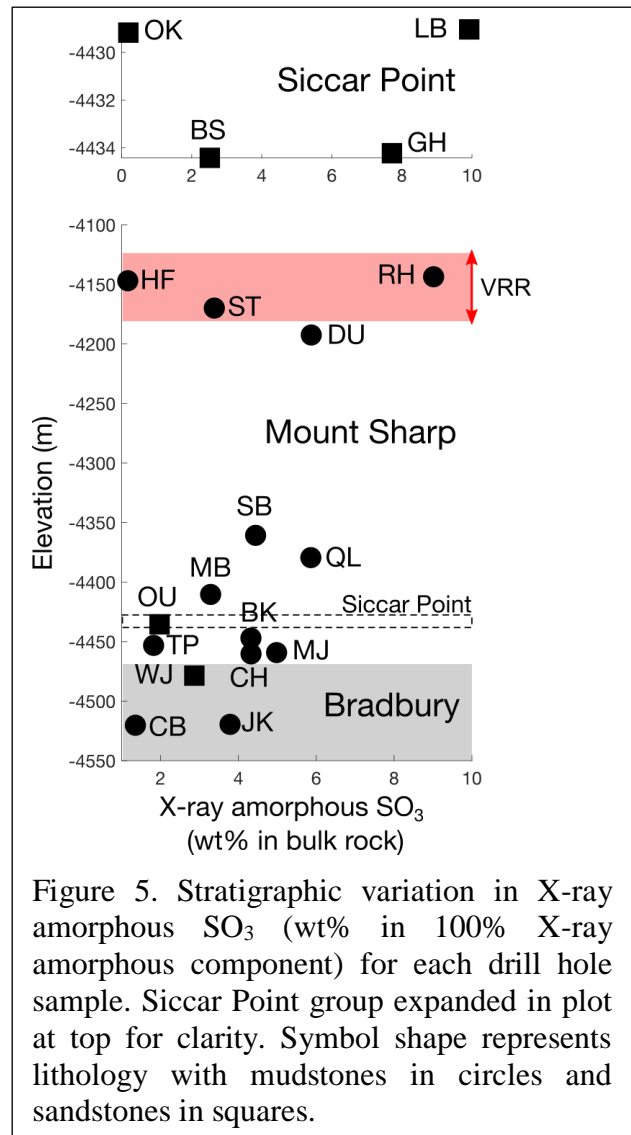


Figure 5. Stratigraphic variation in X-ray amorphous SO₃ (wt% in 100% X-ray amorphous component) for each drill hole sample. Siccar Point group expanded in plot at top for clarity. Symbol shape represents lithology with mudstones in circles and sandstones in squares.

535 and the SO₂ from these samples was attributed to sedimentary sulfides. Most samples have
536 oxidized S-bearing phases such as sulfates and sulfites, indicating mostly oxidizing conditions
537 during the formation of the X-ray amorphous sulfur-bearing phases.

538 Potential oxidized S-bearing phases present in the X-ray amorphous components include
539 crystalline sulfates or sulfites present below the detection limit of CheMin (~1 wt%); amorphous,
540 nanocrystalline, or poorly crystalline sulfates and sulfites; and SO₄²⁻ anions adsorbed onto X-ray
541 amorphous alteration products. Due to instrument limitations, we are unable to definitively
542 determine the crystallinity of the S-bearing phases that make up the X-ray amorphous fraction. In
543 four of the five samples for which we have SAM peak integrations (WJ, CH, MJ2, and GH1),
544 SAM-derived SO₃ associated with Mg-S phases is > 1 wt%, which should be detectable by
545 CheMin if these contents represented a single crystalline Mg-S phase. The fact that they are not
546 detected by CheMin indicates that either this material is amorphous, nanocrystalline, or poorly
547 crystalline or there are multiple crystalline Mg-S phases each present at < ~1 wt%. The same can
548 be said for SAM-derived SO₃ associated with Fe-S phases where present above the detection
549 limit of CheMin. Below we discuss these possibilities.

550 Amorphous, poorly crystalline, and nanocrystalline sulfates have been previously
551 hypothesized for the Martian surface as the current cold and dry environmental conditions are
552 conducive to the formation and preservation of these phases. Amorphous sulfate solids can form
553 through two general means: (1) direct precipitation or (2) structural destabilization of previously
554 crystalline sulfates. Research over the past few decades has shown that most crystalline phases
555 formed at low temperatures have amorphous and nanocrystalline precursors, and Ca-sulfates
556 such as gypsum are no exception (e.g., Wang, Y. et al., 2012; Jia et al., 2020). However,
557 amorphous calcium sulfates have very short lifetimes in laboratory settings and experiments
558 generally produce small quantities (e.g., Wang, Y. et al., 2012; Morris et al., 2015). Morris et al.
559 (2015) found that freeze-drying mixed cation sulfate solutions (e.g., Fe³⁺, Mg²⁺, Na⁺, K⁺) will
560 cryoprecipitate XRD detectable abundances of amorphous sulfates but freeze-drying single
561 cation sulfate solutions (Ca²⁺, K⁺, Na⁺) will not. The complexity of X-ray amorphous sulfur-
562 phase compositions in Gale crater suggest mixed cation solution compositions that might have
563 precipitated greater abundances of amorphous (vs. crystalline) precipitates. However, possibly
564 more likely for Gale crater is the formation of amorphous, poorly crystalline, and nanocrystalline
565 sulfates when hydrated crystalline sulfates experience rapid dehydration, which causes structural
566 destabilization. This has been shown to be an important process for hydrated Mg and Fe-sulfates
567 and could take place upon exposure to surface conditions during erosion or upon exposure to
568 warmer and drier conditions inside the rover instruments during sample measurement (Vaniman
569 et al., 2004; Vaniman and Chipera, 2006; Wang et al., 2009; Wang and Zhou, 2014; Sklute et al.,
570 2015, 2018). However, while gypsum could dehydrate to bassanite and possibly anhydrite under
571 Mars surface conditions (Vaniman et al., 2018), we could find no examples in the literature for
572 the formation of amorphous Ca-sulfates through the structural destabilization of hydrated
573 crystalline Ca-sulfates. Therefore, it is uncertain if the X-ray amorphous Ca-S materials in Gale
574 crater rocks could have formed through dehydration. More work is needed to determine if these
575 X-ray amorphous Ca-S phases are truly present and, if they are present, more work is needed to
576 better understand their formation mechanisms.

577 Sulfate anions can be adsorbed onto X-ray amorphous weathering products, such as
578 allophane and ferrihydrite, in soils on Earth (e.g., Ishiguro et al. 2006) at contents comparable to
579 X-ray amorphous SO₃ contents reported for Gale crater rocks (Jara et al. 2006; Rampe et al.,

2016). These X-ray amorphous weathering product – sulfate complexes would be X-ray amorphous to CheMin if present in Gale crater rocks. Rampe et al. (2016) examined XRD patterns and evolved SO₂ release traces for complexes consisting of sulfate anions chemisorbed onto allophane and ferrihydrite. They found that the sulfate – allophane complex had peak SO₂ releases at temperatures outside the usual temperature range for the SAM instrument, and so this complex would not be detectable by SAM and could be an alternate explanation for the SO₃ interpreted here as amorphous Ca-sulfate. Using the X-ray amorphous Al₂O₃ contents of the samples in this study with SO₃ attributed to amorphous Ca-sulfate (MJ2, BS1, and GH1), we find that 18.7%, 8.5%, and 0.2% of their respective X-ray amorphous components could be comprised of Al-rich allophane. However, we point out that X-ray amorphous Al₂O₃ contents and SO₃ attributed to amorphous Ca-sulfate are seemingly anticorrelated in this sample set (e.g., MJ2 has the lowest abundance of potential amorphous Ca-sulfate and highest potential allophane contribution while GH1 has the highest abundance of potential amorphous Ca-sulfate and the lowest potential allophane contribution). Thus, allophane– sulfate complexes could explain some, but probably not all of the amorphous SO₃ attributed to Ca-S. The sulfate – ferrihydrite complex did evolve SO₂ in the temperature range measured by SAM, but the shape of the trace was inconsistent with that from the Rocknest soil and John Klein samples (Rampe et al., 2016), as well as the subsequent drill holes (e.g., CB, WJ, CH, MJ, TP, BK, BS, and GH) (Sutter et al., 2017). Thus, these specific sulfate anion – X-ray amorphous weathering product complexes are not likely major contributors to the X-ray amorphous SO₃ components in Gale crater rocks, but it is possible that other adsorbed sulfate - X-ray amorphous weathering product complexes are present, given the wide range of X-ray amorphous weathering products found in terrestrial analog sedimentary materials (Smith and Horgan, 2021).

Terrestrial settings are known to have a plethora of crystalline Mg and Fe-sulfate and hydrated sulfate phases, and sulfate phase assemblages can be complex (Chou et al., 2013 and references therein). Laboratory experiments suggest the same may be true for the Martian surface and subsurface (Chou et al., 2013 and references therein), indicating that multiple crystalline oxidized sulfur-bearing phases could be present below the CheMin detection limit. For instance, there is significant overlap in the temperature and relative humidity stability fields for MgSO₄ • 1H₂O, MgSO₄ • 4H₂O, and amorphous MgSO₄ • nH₂O (Chou et al., 2013), suggesting multiple crystalline hydrates could be present and could also be intimately mixed with amorphous Mg-sulfates.

Possible reduced S-bearing phases contributing to the X-ray amorphous S-bearing material are crystalline sulfide phases present below the detection limit of CheMin and S-bearing inclusions in minerals or glass (McAdam et al., 2014; Sutter et al., 2017). SAM can detect the pyrolysis of reduced sulfur-bearing phases, and some of the samples have at least one SO₂ peak consistent with oxidized elemental sulfur or sulfides (CB and MJ2) (Franz et al., 2017). Petrographic analyses of Martian meteorites show that the Martian crust contains a range of reduced S-bearing phases such as pyrrhotite, rare chalcopyrite and/or cubanite, pentlandite, troilite-pentlandite-chalcopyrite intergrowths, pyrite, and some secondary marcasite (Meyer 2008 and references therein). Collectively, these phases compose a minor component of the Martian crust, with S present at < 1 wt% (equivalent to 2.0 wt% SO₂ and 2.5 wt% SO₃). Ion microprobe analyses of primitive shergottite meteorites indicate that sulfur is present in mineral-hosted melt inclusions at < ~0.2 wt% (equivalent to 0.4 wt% SO₂ and 0.5 wt% SO₃) and in groundmass glass at < ~0.6 wt% (equivalent to 1.2 wt% SO₂ and 1.5 wt% SO₃) (Usui et al., 2012). These observations indicate that oxidation of reduced S-phases in melt inclusions and groundmass glass

626 could collectively produce up to ~ 1.6 wt% of the SAM evolved SO₂ (~2.0 wt% SO₃) in any
627 sample. These minor phases could account for the relatively small X-ray amorphous S-bearing
628 material contents of the Cumberland (CB) sample (1.4 wt%) and the small low temperature SO₂
629 peak for Mojave2 (MJ2), as shown in Franz et al. (2017). Note that if present at these fractions,
630 elemental sulfur and sulfides should be detected by both the SAM and APXS instruments, so
631 these phases cannot explain the ΔSO₃ that we attribute to Ca-S.

632

633 5.2 Relative timing of deposition

634 X-ray amorphous SO₃ contents show no strong correlation with either X-ray amorphous
635 SiO₂ or FeO_T, unlike the anticorrelation observed between X-ray amorphous SiO₂ and FeO_T
636 contents as reported by Smith et al. (2021). Additionally, X-ray amorphous SO₃ content does not
637 change across the Bradbury Group - Mount Sharp boundary. Previous studies have shown
638 evidence for changes in sediment source (Bedford et al., 2019) and increased chemical alteration
639 (e.g., Mangold et al., 2019) across this boundary, and the observation that X-ray amorphous SiO₂
640 increased across the boundary was used as evidence to hypothesize that the X-ray amorphous
641 SiO₂ was also linked to the sediment source regions for many Bradbury and Mount Sharp group
642 rocks (Smith et al., 2021). The lack of correlation between X-ray amorphous SO₃ and source
643 regions indicates that X-ray amorphous SO₃ deposition was, for the most part, (i) unrelated to the
644 deposition of X-ray amorphous SiO₂ and FeO_T, (ii) that SO₃ concentrations were much more
645 variable than SiO₂ in the source rocks or fluids that deposited the X-ray amorphous materials,
646 and/or (iii) that later diagenetic fluids introduced new SO₃ or mobilized and redistributed SO₃,
647 overprinting any original correlation with the other X-ray amorphous component constituents.

648 Observations of most of the Bradbury and Mount Sharp group locations covered in this
649 study indicate that late-stage diagenetic fluids were primarily confined to fractures. For the most
650 part, sharp contacts between mineral infilling and host rock indicate that the sediments were well
651 lithified before the formation of the fractures (De Toffoli et al., 2020) and there is no evidence
652 that the sulfur-bearing diagenetic fluids permeated the surrounding bedrock. APXS studies
653 consistently find that vein-bearing targets have CaO:SO₃ weight ratios of ~3:2, consistent with
654 Ca-sulfate (Berger et al., 2020). Additionally, a comparison of measured areas of light-toned
655 veins in the Cumberland and John Klein bore holes with the CheMin Ca-sulfate abundances
656 indicate that most, if not all of the XRD-detected Ca-sulfates at these locations could be
657 associated with such visible diagenetic features (e.g., Vaniman et al. 2014). Thus, if the X-ray
658 amorphous S-bearing materials reside in the bedrock, as is likely since there is no indication of
659 large, continuous salt deposits (Rapin et al., 2019), the simplest conclusion is that the X-ray
660 amorphous S-bearing materials were deposited before the diagenetic veins. Fractures and
661 diagenetic veins are interpreted to have formed mostly during late diagenesis (post cementation)
662 (e.g., Nachon et al., 2014, 2017; Rapin et al., 2016; Kronyak et al., 2019; De Toffoli et al., 2020)
663 and so the X-ray amorphous SO₃ would have been deposited either with the detrital sediments
664 (syn-depositional) or during early diagenesis, possibly contributing to sediment cementation.

665 Sulfate cements have been hypothesized for Gale crater rocks in previous studies (e.g.,
666 Blaney et al., 2014; Newsom et al., 2016; Rapin et al., 2019). APXS measurements have shown
667 many instances where Gale crater bedrock has SO₃:CaO ratios that trend away from the simple
668 addition of Ca-sulfate, indicating the presence of other cation sulfur-bearing phases (Berger et
669 al., 2020). Dendritic and spherical concretions (cemented features) often show a positive
670 correlation between MgO and SO₃ and could be enriched with ~10-15 wt% pure MgSO₄

671 (VanBommel et al., 2016, 2017). Thus, Berger et al. (2020) hypothesized that some Mg-sulfate
672 could also be present in the bedrock matrix, likely at abundances equal to or lower than Mg-
673 sulfate in the concretions, which is consistent with bedrock Mg-sulfate abundances determined in
674 this study. While the ChemCam LIBS instrument does not quantify volatiles (e.g., S, H, C and P)
675 directly, their presence can be inferred from low oxide totals that indicate “missing components”
676 and peaks in the LIBS spectra (see Nachon et al., 2014 for an in-depth discussion). ChemCam
677 data were used to hypothesize the presence of impure Ca-sulfate cements for sections of the
678 Missoula interval, which belongs to the Stimson formation in the Siccar Point group (Newsom et
679 al., 2016). The Missoula member was not sampled by CheMin, and so there is no information
680 about the crystallinity of the ChemCam-detected Ca-sulfate cement. The nearest unaltered
681 Stimson drill hole locations are Okoruso (OK) and Big Sky (BS), which were sampled at a
682 slightly higher elevation in the Stimson formation. Okoruso has negligible X-ray amorphous
683 SO₃, but SAM analyses indicate that Big Sky has a significant X-ray amorphous Ca-sulfate
684 component that could be consistent with the ChemCam observations. Rapin et al. (2019) also
685 used ChemCam data to show evidence for Ca-sulfate-enriched bedrock in the Sutton Island and
686 Blunts Point members of the Murray formation, with a ~10 m-thick section of possibly Mg-
687 sulfate-enriched bedrock in the Sutton Island member. The base of the Sutton Island member
688 was sampled at Sebina (SB) and the upper section of the Blunts Point member was sampled at
689 Duluth (DU); both samples have X-ray amorphous component compositions that lie relatively
690 close to the tie-line between kieserite and gypsum on the ternary diagram in Figure 3a, and could
691 be consistent with ChemCam observations of Ca- and Mg-sulfate cements. However, the
692 enrichments estimated by Rapin et al. (2019) (30-50 wt% Ca-sulfate and ~25 wt% Mg-sulfate)
693 far exceed X-ray amorphous Ca and Mg-sulfate values estimated for Sebina and Duluth drill
694 holes in this study (0-5.5 wt% and 1-5.5 wt%, respectively; Table DR6). This discrepancy could
695 possibly be a result of the distance between the sites observed with ChemCam and the drill sites.

696 Late diagenetic overprinting has been observed in multiple locations along the rover
697 traverse (discussed in Section 2.1, above), and the samples from these locations have some of the
698 highest and lowest X-ray amorphous SO₃ contents. For example, the two drill hole locations that
699 represent the light-toned, silica-rich alteration “halos” sampled in the Siccar Point group (LB and
700 GH) have some of the highest X-ray amorphous (this study) and crystalline SO₃ contents (Yen et
701 al., 2017) observed. Additionally, the results from our study suggest that the X-ray amorphous
702 and crystalline sulfur-bearing phases in the alteration halos have similar compositions, both
703 being Ca-sulfate-rich. It is unclear how the crystalline and X-ray amorphous S-bearing phases in
704 the alteration halos are related, if at all. Do their similar compositions indicate that crystalline
705 Ca-sulfate deposited during late diagenesis was later partially altered to become X-ray
706 amorphous or that the X-ray amorphous Ca-sulfates represent amorphous precursors that have
707 yet to be converted to more crystalline phases? Interestingly, our SAM data analyses suggest that
708 the composition of the X-ray amorphous S-bearing material in the unaltered bedrock surrounding
709 the halos (BS) is also predominantly Ca-sulfate. The relationship, if any, between the X-ray
710 amorphous S-bearing material in the host rock and the alteration halos remains unclear. The
711 Siccar Point group rocks are sandstones (Banham et al., 2018) and are likely relatively
712 permeable, so it is possible that halo-forming late-diagenetic fluids infiltrated the surrounding
713 bedrock to precipitate the X-ray amorphous Ca-sulfate.

714 Some VRR locations also have strong evidence for late-stage diagenetic overprinting.
715 The Rock Hall (RH) and Highfield (HF) samples represent portions of VRR bedrock that display
716 “red” and “grey” coloring, respectively. The difference in coloring has been attributed to

717 differences in hematite grain size stemming from differences in diagenetic fluid interactions,
718 with red colors resulting from the syn-depositional or early diagenetic formation of fine-grained
719 ferric species, and the gray colors resulting from late-stage diagenetic alteration by groundwater
720 to coarser-grained iron species (e.g., L'Haridon et al., 2020). As such, the Highfield location is
721 thought to have experienced more late-stage diagenetic alteration, and so the low X-ray
722 amorphous SO₃ contents could have resulted from the removal or recrystallization of any X-ray
723 amorphous SO₃, or could suggest that the VRR late-stage diagenetic fluids were less sulfur-
724 bearing than the fluids that formed the alteration “halos” in the Siccar Point group. In contrast,
725 the Rock Hall sample has high X-ray amorphous SO₃ contents that are comparable to those in the
726 Siccar Point group alteration “halos” and has very high abundances of crystalline Ca-sulfates
727 (anhydrite) and minor jarosite (Rampe et al., 2020b), all of which indicate sulfur-rich fluid
728 interactions at this VRR location at one point in time. These X-ray amorphous SO₃ observations
729 are further evidence for spatially variable mobilization and redeposition of geochemical
730 components with diagenetic fluid activity within Gale crater.

731

732 5.3 Consequences for Gale crater environmental conditions

733 Mass balance calculation results coupled with SAM SO₂ EGA trace analyses indicate that
734 in most cases, X-ray amorphous S-bearing materials are complex/intimate mixtures of Mg-S, Fe-
735 S, and possibly Ca-S phases that are likely oxidized (sulfates or sulfites) with reduced S phases
736 as possible low-level contributors. If these X-ray amorphous S-bearing materials are aqueously
737 deposited sulfates and sulfites, what implications do they have for the compositions of fluids in
738 Gale crater? Additionally, if they are amorphous, nanocrystalline, and/or poorly crystalline
739 sulfates, what can these materials tell us about post-depositional environmental conditions?

740 A hypothesis for the formation of sulfate and sulfite evaporite deposits in Gale crater
741 sedimentary rocks involves the concentration and evaporation of brines derived from basaltic
742 weathering during early diagenesis (Rapin et al., 2019). Terrestrial studies show that an
743 important parameter responsible for brine compositions and evaporite mineral assemblages is the
744 composition of the dilute water at the onset of concentration (Hardie and Eugster, 1970). The
745 mostly basaltic crust of Mars coupled with high sulfur contents would produce fluids rich in Mg,
746 Ca, Fe (depending on redox conditions and pH), SiO₂, and SO₃ compared to weathering
747 solutions on Earth (e.g., Burns 1993; Catling 1999; King and McLennan, 2010). Modeling
748 efforts have shown that the evaporite mineralogy precipitated from such Martian weathering
749 solutions would be dominated by Mg, Fe (depending on redox conditions and pH), Ca-sulfates
750 and silica phases such as amorphous silica (Tosca and McLennan, 2006).

751 Compared to other sulfate assemblages examined in situ on Mars, including crystalline,
752 amorphous, or phases of unknown crystalline state, Gale crater rocks seem to have relatively less
753 Fe-S phases and more Mg-S and Ca-S phases. Crystalline Fe-sulfate (jarosite) was detected in
754 eight of the nineteen drill hole locations examined in this study at ~1-3 wt% in the bulk rock
755 (Table 1; Rampe et al., 2020a), and X-ray amorphous Fe-S phases were found to be relatively
756 significant in two of the five rocks examined in this study using detailed SAM analyses (CH and
757 MJ2). In contrast, the instrument suite of the Opportunity rover determined that the Burns
758 formation of Meridiani Planum consisted of ~10 wt% jarosite (via combined APXS and
759 Mössbauer), ~18 wt% Mg-sulfate, and ~10 wt% Ca-sulfate (via APXS and TIR spectroscopy)
760 (Clark et al., 2005; McLennan and Grotzinger, 2008). Since this study examined only a small
761 subset of samples with detailed SAM analyses, it is unclear how important amorphous Fe-S

762 phases are in Gale crater rocks. Future studies with larger sample sets are necessary to better
763 determine the spatial and temporal variability of crystalline and amorphous Mg, Fe, and Ca
764 phase ratios below and through the mineral transition. Such work can help constrain changes in
765 environmental conditions in Gale crater that can be compared to other rover landing sites.

766 The relative rarity of crystalline or X-ray amorphous Fe-S at some Gale crater drill hole
767 locations (e.g., WJ, BS and GH) could be a result of environmental factors (pH, temperature)
768 and/or parent rock lithology different from other locations on Mars. Ferric and ferrous iron
769 sulfates, such as jarosite and melanterite, typically form in acidic environments on Earth (e.g.,
770 Cogram, 2018). For example, at 298 K, jarosite is stable between pH ~2.5 to 3.5 under oxidizing
771 conditions (e.g., Elwood Madden et al., 2004). Tosca et al. (2005) modeled evaporite
772 assemblages of different weathering fluids relevant for Mars and showed that weathering fluids
773 with pH > 3.5 will not produce jarosite, and at slightly higher pH levels, fluids will precipitate
774 the poorly crystalline Fe-hydroxysulfate schwertmannite (pH ~2.5-6) (Tosca et al., 2005). Thus,
775 the lack of both crystalline and X-ray amorphous Fe-S phases at these locations could indicate a
776 near-neutral fluid pH (> ~6). Alternatively, weathering solutions could have been more acidic,
777 initially precipitating jarosite, but with continued diagenetic fluid interactions, jarosite would
778 eventually breakdown to form goethite (Tosca et al., 2005). No goethite has been detected at any
779 of the drill hole locations in this study, but goethite can alter over time with continued diagenetic
780 fluid interactions to form hematite. However, this seems to be an unlikely pathway for Gale
781 crater as continued diagenetic fluid interactions would also likely have recrystallized the
782 amorphous SiO₂ and FeO_T phases found in high abundance in nearly all drill hole locations
783 (Smith et al., 2021).

784 An alternative explanation for the presence of X-ray amorphous S-bearing phases in the
785 bedrock (as opposed to having been precipitated from weathering fluids during early diagenesis)
786 is their emplacement by brines originating from the overlying sulfate-bearing unit that is detected
787 from orbit. Bristow et al. (2021) argue that the emplacement of the aerially extensive and thick
788 sulfate-bearing unit would have caused density-driven brine infiltration into the underlying
789 Mount Sharp group sediments prior to lithification. The brines would have been silica-poor,
790 which could have promoted the destabilization of detrital feldspar and Fe-bearing clay minerals,
791 forming X-ray amorphous silica and iron-bearing materials and depositing Mg and Ca-sulfates
792 (Bristow et al., 2021).

793 Materials originally precipitated as amorphous should easily dissolve or recrystallize into
794 crystalline materials with time, heat, and water, and this would especially be the case for such
795 soluble phases as sulfates. In fact, laboratory crystallization experiments have shown that
796 amorphous Ca-sulfate precursors form faceted gypsum crystals after ~40 minutes at 90°C (Jia et
797 al., 2021). Thus, it would be very surprising if these are primary (~3-4 Ga) materials that stayed
798 amorphous during burial in Gale crater. More likely, these X-ray amorphous phases represent
799 multiple crystalline S-bearing phases each present below the detection limit of CheMin or phases
800 that more recently became amorphous through partial dehydration, as has been shown to happen
801 for epsomite (Vaniman et al., 2004; Vaniman and Chipera, 2006; Wang et al., 2009) and
802 hydrated Fe-sulfates (Wang and Zhou, 2014; Sklute et al., 2015, 2018). Hydrous evaporative
803 phases initially deposited as crystalline could have become amorphized when exposed through
804 erosion to surface conditions or by the rover to instrument conditions.

805 Regardless of crystallinity, Mg-sulfates are the most soluble of the three mono-cation
806 sulfates considered here (Ca, Mg, and Fe-sulfates), and any post-depositional interactions with
807 dilute meteoric surface or ground waters would have caused preferential dissolution of the Mg-
808 sulfates. Because of their solubility, the fact that the X-ray amorphous S-bearing components of
809 many Mount Sharp group rocks are seemingly dominated by Mg-sulfates suggests negligible
810 fluid flow through the bulk bedrock post-Mg-sulfate deposition at these locations. It should be
811 noted that the presence of 2.1 Ga jarosite in the Mojave2 bedrock sample (Martin et al., 2017),
812 which also contains a large fraction of X-ray amorphous Mg-S phases, indicates some fluid
813 interactions long past sediment lithification. The question is whether or not this jarosite is
814 representative of more pervasive late diagenetic fluids infiltrating bedrock throughout Gale crater
815 or if it formed through very localized reactions. The fact that jarosite is not detected in more drill
816 sites is an argument in support of more localized processes.

817

818 **6 Implications**

819 Hydrated amorphous sulfates have visible and near infrared (VNIR) spectral features at
820 the same positions as their crystalline counterparts (Wang, A. et al., 2009), and so the crystalline
821 state of hydrated Mg-sulfates detected from orbit cannot be discerned. Spectral maps from
822 Milliken et al. (2010), Fraeman et al. (2016) and Sheppard et al., (2021a) show that most of the
823 rocks traversed by the rover through sol 2300 have been spectrally bland, have shown
824 phyllosilicate spectral signatures mixed with weak hydrated Mg-sulfate spectral signatures, or
825 have been consistent with mafic minerals that might have obscured or weakened sulfate spectral
826 signatures. This study used in situ investigations from the Curiosity rover to confirm that the
827 sedimentary rocks of Gale crater from the landing site through VRR contain Mg-S phases, most
828 likely Mg-sulfates intimately mixed with Fe and Ca-sulfates, all of which appear X-ray
829 amorphous to CheMin.

830 The rocks higher up Mount Sharp in the “sulfate unit” have much stronger hydrated Mg-
831 sulfate spectral signatures and the reasons for the increase in spectral signature strength have yet
832 to be discovered (Milliken et al., 2010; Sheppard et al., 2021a). Several hypotheses regarding
833 this transition can be tested as the rover enters the sulfate unit. One hypothesis is that, regardless
834 of crystalline state, Mg-sulfate contents are higher in the sulfate unit with relatively fewer mafic
835 minerals to mask the sulfate spectral signatures. Such a finding would indicate a more saline or
836 less water-dominated environment. A second hypothesis is that the range of Mg-sulfate contents
837 does not change significantly across the transition, but the sulfate-bearing unit is less dusty,
838 allowing for a stronger bedrock signature to reach the orbiting spectrometer. A third hypothesis
839 is that the range of Mg-sulfate contents does not change significantly across the transition, but
840 there is an increase in crystallinity or hydration state in the sulfate unit resulting from a
841 difference in exposure to Martian surface conditions. The spectral contrast of hydrated sulfates
842 decreases with decreasing crystallinity and hydration, which would make amorphous phases
843 more challenging to detect, especially when present in mixtures with strong absorbers (Sheppard
844 et al., 2021b). Lastly, the presence of > ~10 wt% clay minerals has been shown to obscure the
845 spectral signature of amorphous Mg-sulfates (Sheppard et al., 2021a), and so a fourth hypothesis
846 is that clay minerals are not present (or present at low abundance) in the sulfate unit. Clay
847 minerals have been detected at most drill hole locations in this study, and so a decrease in clay
848 minerals would indicate a major shift in environment, during weathering in the source region or
849 during diagenesis, depending on whether the clay minerals are detrital or diagenetic (Bridges et
850 al., 2015; Bristow et al., 2018), or could also possibly indicate the destruction of once present

851 clay minerals through diagenetic alteration (Bristow et al., 2021). Testing these hypotheses will
852 be important for understanding the evolution of the Martian surface environment and climate at
853 Gale crater.

854
855 **Acknowledgments:** There are no real or perceived financial conflicts of interests for any author.
856 All data supporting the conclusions can be obtained within the article and in the referenced
857 published work, or in the Supplemental Material (Smith R., 2021) found here:
858 <http://dx.doi.org/10.17632/8b5yj38wx3.1>. This work was funded through a NASA Participating
859 Scientist award to SMM (JPL Subcontract 1457128). A portion of this research was carried out
860 at the Jet Propulsion Laboratory, California Institute of Technology, under a contract with the
861 National Aeronautics and Space Administration (80NM0018D0004). The authors are indebted to
862 the MSL science, engineering, and management teams for their efforts in tactical and strategic
863 operations.

864

865 **References**

866

867 Achilles, C. N., Rampe, E. B., Downs, R. T., Bristow, T. F., Ming, D. W., Morris, R. V.,
868 Vaniman, D. T., Blake, D. F., et al. (2020). Evidence for Multiple Diagenetic Episodes in
869 Ancient Fluvial-Lacustrine Sedimentary Rocks in Gale Crater, Mars. *Journal of*
870 *Geophysical Research: Planets*, 125(8). <https://doi.org/10.1029/2019JE006295>

871

872 Archer, P. D., Ming, D. W., & Sutter, B. (2013). The effects of instrument parameters and
873 sample properties on thermal decomposition: Interpreting thermal analysis data from
874 Mars. *Planetary Science*, 2(1), 2. <https://doi.org/10.1186/2191-2521-2-2>

875

876 Banham, S. G., Gupta, S., Rubin, D. M., Watkins, J. A., Sumner, D. Y., Edgett, K. S.,
877 Grotzinger, J. P., Lewis, K. W., et al. (2018). Ancient Martian aeolian processes and
878 palaeomorphology reconstructed from the Stimson formation on the lower slope of
879 Aeolis Mons, Gale crater, Mars. *Sedimentology*, 65(4), 993–1042.
880 <https://doi.org/10.1111/sed.12469>

881

882 Bedford, C. C., Bridges, J. C., Schwenzer, S. P., Wiens, R. C., Rampe, E. B., Frydenvang, J., &
883 Gasda, P. J. (2019). Alteration trends and geochemical source region characteristics
884 preserved in the fluvio-lacustrine sedimentary record of Gale crater, Mars. *Geochimica et*
885 *Cosmochimica Acta*, 246, 234–266. <https://doi.org/10.1016/j.gca.2018.11.031>

886

887 Berger, J. A., Gellert, R., Boyd, N. I., King, P. L., McCraig, M. A., O'Connell-Cooper, C. D.,
888 Schmidt, M. E., Spray, J. G., et al. (2020). Elemental Composition and Chemical
889 Evolution of Geologic Materials in Gale Crater, Mars: APXS Results From Bradbury
890 Landing to the Vera Rubin Ridge. *Journal of Geophysical Research: Planets*, 125(12).
891 <https://doi.org/10.1029/2020JE006536>

892

893 Bibring, J.-P., Langevin, Y., Mustard, J. F., Poulet, F., Arvidson, R., Gendrin, A., Gondet, B.,
894 Mangold, N., et al. (2006). Global Mineralogical and Aqueous Mars History Derived
895 from OMEGA/Mars Express Data. *Science*, 312(5772), 400–404.
896 <https://doi.org/10.1126/science.1122659>

897
898 Blake, D., Vaniman, D., Achilles, C., Anderson, R., Bish, D., Bristow, T., Chen, C., Chipera, S.,
899 et al. (2012). Characterization and Calibration of the CheMin Mineralogical Instrument
900 on Mars Science Laboratory. *Space Science Reviews*, 170(1–4), 341–399.
901 <https://doi.org/10.1007/s11214-012-9905-1>
902
903 Blaney, D. L., Wiens, R. C., Maurice, S., Clegg, S. M., Anderson, R. B., Kah, L. C., Le Mouélic,
904 S., Ollila, A., et al. (2014). Chemistry and texture of the rocks at Rocknest, Gale Crater:
905 Evidence for sedimentary origin and diagenetic alteration: Rocknest Chemistry and
906 Texture. *Journal of Geophysical Research: Planets*, 119(9), 2109–2131.
907 <https://doi.org/10.1002/2013JE004590>
908
909 Bridges, J. C., Schwenzer, S. P., Leveille, R., Westall, F., Wiens, R. C., Mangold, N., Bristow,
910 T., Edwards, P., et al. (2015). Diagenesis and clay mineral formation at Gale Crater,
911 Mars: Gale Crater Diagenesis. *Journal of Geophysical Research: Planets*, 120(1), 1–19.
912 <https://doi.org/10.1002/2014JE004757>
913
914 Bristow, T. F., Bish, D. L., Vaniman, D. T., Morris, R. V., Blake, D. F., Grotzinger, J. P.,
915 Rampe, E. B., Crisp, J. A., et al. (2015). The origin and implications of clay minerals
916 from Yellowknife Bay, Gale crater, Mars. *American Mineralogist*, 100(4), 824–836.
917 <https://doi.org/10.2138/am-2015-5077CCBYNCND>
918
919 Bristow, T. F., Grotzinger, J. P., Rampe, E. B., Cuadros, J., Chipera, S. J., Downs, G. W., Fedo,
920 C. M., Frydenvang, J., et al. (2021). Brine-driven destruction of clay minerals in Gale
921 crater, Mars. *Science*, 373(6551), 198–204. <https://doi.org/10.1126/science.abg5449>
922
923 Bristow, T. F., Rampe, E. B., Achilles, C. N., Blake, D. F., Chipera, S. J., Craig, P., Crisp, J. A.,
924 Des Marais, D. J., et al. (2018). Clay mineral diversity and abundance in sedimentary
925 rocks of Gale crater, Mars. *Science Advances*, 4(6), eaar3330.
926 <https://doi.org/10.1126/sciadv.aar3330>
927
928 Burns, R.G. (1993) Rates and mechanisms of chemical weathering of ferromagnesian silicate
929 minerals on Mars, *Geochimica et Cosmochimica Acta*, Volume 57, Issue 19, 1993, Pages
930 4555-4574, ISSN 0016-7037, [https://doi.org/10.1016/0016-7037\(93\)90182-V](https://doi.org/10.1016/0016-7037(93)90182-V).
931
932 Carter, J., Poulet, F., Bibring, J.-P., Mangold, N., & Murchie, S. (2013). Hydrous minerals on
933 Mars as seen by the CRISM and OMEGA imaging spectrometers: Updated global view:
934 hydrous minerals on mars: Global view. *Journal of Geophysical Research: Planets*,
935 118(4), 831–858. <https://doi.org/10.1029/2012JE004145>

936 Catling, D. C. (1999). A chemical model for evaporites on early Mars: Possible sedimentary
937 tracers of the early climate and implications for exploration. *Journal of Geophysical*
938 *Research: Planets*, 104(E7), 16453–16469. <https://doi.org/10.1029/1998JE001020>

939 Chou, I-M., Seal, R. R., and Wang, A. (2013). The stability of sulfate and hydrated sulfate
940 minerals near ambient conditions and their significance in environmental and planetary

- 941 sciences. *Journal of Asian Earth Sciences*, 62, 734-758. [https://](https://doi.org/10.1016/j.jseaes.2012.11.027)
942 10.1016/j.jseaes.2012.11.027
- 943 Clark, B. C., Morris, R. V., McLennan, S. M., Gellert, R., Jolliff, B., Knoll, A. H., Squyres, S.
944 W., Lowenstein, T. K., et al. (2005). Chemistry and mineralogy of outcrops at Meridiani
945 Planum. *Earth and Planetary Science Letters*, 240(1), 73–94.
946 <https://doi.org/10.1016/j.epsl.2005.09.040>
- 947 Cogram, P. (2018). Jarosite. Reference Module in Earth Systems and Environmental Sciences.
948 Elsevier. doi: [10.1016/B978-0-12-409548-9.10960-1](https://doi.org/10.1016/B978-0-12-409548-9.10960-1)
- 949 David, G., Cousin, A., Forni, O., Meslin, P. -Y., Dehouck, E., Mangold, N., L'Haridon, J.,
950 Rapin, W., et al. (2020). Analyses of High-Iron Sedimentary Bedrock and Diagenetic
951 Features Observed With ChemCam at Vera Rubin Ridge, Gale Crater, Mars: Calibration
952 and Characterization. *Journal of Geophysical Research: Planets*, 125(10).
953 <https://doi.org/10.1029/2019JE006314>
- 954 Dehouck, E., McLennan, S. M., Meslin, P.-Y., & Cousin, A. (2014). Constraints on abundance,
955 composition, and nature of X-ray amorphous components of soils and rocks at Gale
956 crater, Mars: X-ray amorphous components at Gale. *Journal of Geophysical Research:*
957 *Planets*, 119(12), 2640–2657. <https://doi.org/10.1002/2014JE004716>
- 958 Dehouck, E., McLennan, S. M., Sklute, E. C., & Dyar, M. D. (2017). Stability and fate of
959 ferrihydrite during episodes of water/rock interactions on early Mars: An experimental
960 approach: Stability of Ferrihydrite on Early Mars. *Journal of Geophysical Research:*
961 *Planets*, 122(2), 358–382. <https://doi.org/10.1002/2016JE005222>
- 962 Elwood Madden et al., 2004
- 963 Fraeman, A. A., Edgar, L. A., Rampe, E. B., Thompson, L. M., Frydenvang, J., Fedo, C. M.,
964 Catalano, J. G., Dietrich, W. E., et al. (2020). Evidence for a Diagenetic Origin of Vera
965 Rubin Ridge, Gale Crater, Mars: Summary and Synthesis of *Curiosity* 's Exploration
966 Campaign. *Journal of Geophysical Research: Planets*, 125(12).
967 <https://doi.org/10.1029/2020JE006527>
- 968 Fraeman, A. A., Ehlmann, B. L., Arvidson, R. E., Edwards, C. S., Grotzinger, J. P., Milliken, R.
969 E., Quinn, D. P., & Rice, M. S. (2016). The stratigraphy and evolution of lower Mount
970 Sharp from spectral, morphological, and thermophysical orbital data sets: Stratigraphy
971 and Evolution of Mount Sharp. *Journal of Geophysical Research: Planets*, 121(9), 1713–
972 1736. <https://doi.org/10.1002/2016JE005095>
- 973 Franz, H. B., McAdam, A. C., Ming, D. W., Freissinet, C., Mahaffy, P. R., Eldridge, D. L.,
974 Fischer, W. W., Grotzinger, J. P., et al. (2017). Large sulfur isotope fractionations in
975 Martian sediments at Gale crater. *Nature Geoscience*, 10(9), 658–662.
976 <https://doi.org/10.1038/ngeo3002>
- 977 Frydenvang, J., Gasda, P. J., Hurowitz, J. A., Grotzinger, J. P., Wiens, R. C., Newsom, H. E.,
978 Edgett, K. S., Watkins, J., et al. (2017). Diagenetic silica enrichment and late-stage

- 979 groundwater activity in Gale crater, Mars: Silica Enriching Diagenesis, Gale, Mars.
980 *Geophysical Research Letters*, 44(10), 4716–4724.
981 <https://doi.org/10.1002/2017GL073323>
982
- 983 Gabriel, T. S. J., Hardgrove, C., Achilles, C., Rampe, E. B., Czarnecki, S., Rapin, W., Nowicki,
984 S., Thompson, L. M., et al. (2019) Pervasive water-rich, fracture-associated alteration
985 halos in Gale crater, Mars. American Geophysical Union, Fall Meeting 2019, abstract
986 #P43B-08
- 987 Grant, J. A., Wilson, S. A., Mangold, N., Calef, F., & Grotzinger, J. P. (2014). The timing of
988 alluvial activity in Gale crater, Mars. *Geophysical Research Letters*, 41(4), 1142–1149.
989 <https://doi.org/10.1002/2013GL058909>
- 990 Grotzinger, J. P., Gupta, S., Malin, M. C., Rubin, D. M., Schieber, J., Siebach, K., Sumner, D.
991 Y., Stack, K. M., et al. (2015). Deposition, exhumation, and paleoclimate of an ancient
992 lake deposit, Gale crater, Mars. *Science*, 350(6257), aac7575–aac7575.
993 <https://doi.org/10.1126/science.aac7575>
- 994 Grotzinger, J. P., Sumner, D. Y., Kah, L. C., Stack, K., Gupta, S., Edgar, L., Rubin, D., Lewis,
995 K., et al. (2014). A Habitable Fluvio-Lacustrine Environment at Yellowknife Bay, Gale
996 Crater, Mars. *Science*, 343(6169), 1242777–1242777.
997 <https://doi.org/10.1126/science.1242777>
- 998 Hardie, L. W. A., & Eugster, H. P. (1970). The Evolution of Closed-Basin Brines. *Mineralogical*
999 *Society of America Special Paper*, 3, 273–290.
- 1000 Hausrath, E. M., Ming, D. W., Peretyazhko, T. S., & Rampe, E. B. (2018). Reactive transport
1001 and mass balance modeling of the Stimson sedimentary formation and altered fracture
1002 zones constrain diagenetic conditions at Gale crater, Mars. *Earth and Planetary Science*
1003 *Letters*, 491, 1–10. <https://doi.org/10.1016/j.epsl.2018.02.037>
- 1004 Horgan, B. H. N., Johnson, J. R., Fraeman, A. A., Rice, M. S., Seeger, C., Bell, J. F., Bennett, K.
1005 A., Cloutis, et al. (2020). Diagenesis of Vera Rubin Ridge, Gale Crater, Mars, From
1006 Mastcam Multispectral Images. *Journal of Geophysical Research: Planets*, 125(11).
1007 <https://doi.org/10.1029/2019JE006322>
- 1008 Hurowitz, J. A., Grotzinger, J. P., Fischer, W. W., McLennan, S. M., Milliken, R. E., Stein, N.,
1009 Vasavada, A. R., Blake, D. F., et al. (2017). Redox stratification of an ancient lake in
1010 Gale crater, Mars. *Science*, 356(6341), eaah6849.
1011 <https://doi.org/10.1126/science.aah6849>
- 1012 Ishiguro, M., Makino, T., & Hattori, Y. (2006). Sulfate adsorption and surface precipitation on a
1013 volcanic ash soil (allophanic andisol). *Journal of Colloid and Interface Science*, 300(2),
1014 504–510. <https://doi.org/10.1016/j.jcis.2006.04.032>
- 1015 Jara, A.A., Violante, A., Pigna, M., and de la Luz Mora, M. (2006). Mutual interactions of
1016 sulfate, oxalate, citrate, and phosphate on synthetic and natural allophanes. *Soil Science*
1017 *Society of America Journal*, 70, 337–346.

- 1018 Jia, C., Wu, L., Chen, Q., Ke, P., De Yoreo, J. J., & Guan, B. (2020). Structural evolution of
1019 amorphous calcium sulfate nanoparticles into crystalline gypsum phase. *CrystEngComm*,
1020 22(41), 6805–6810. <https://doi.org/10.1039/D0CE01173H>
- 1021 Jia, C., Wu, L., Fulton, J. L., Liang, X., De Yoreo, J. J., & Guan, B. (2021). Structural
1022 Characteristics of Amorphous Calcium Sulfate: Evidence to the Role of Water
1023 Molecules. *The Journal of Physical Chemistry C*, 125(6), 3415–3420.
1024 <https://doi.org/10.1021/acs.jpcc.0c10016>
- 1025 Kah, L. C., Stack, K. M., Eigenbrode, J. L., Yingst, R. A., & Edgett, K. S. (2018).
1026 Syndepositional precipitation of calcium sulfate in Gale Crater, Mars. *Terra Nova*, 30(6),
1027 431–439. <https://doi.org/10.1111/ter.12359>
- 1028 King, P. L., & McLennan, S. M. (2010). Sulfur on Mars. *Elements*, 6 (2), 107–112. doi:
1029 <https://doi.org/10.2113/gselements.6.2.107>
- 1030 Klug, H. P., & Alexander, L. E. (1974). X-ray diffraction procedures: For polycrystalline and
1031 amorphous materials (2nd ed.). John Wiley and Sons.
- 1032 Kronyak, R. E., Kah, L. C., Miklusick, N. B., Edgett, K. S., Sun, V. Z., Bryk, A. B., &
1033 Williams, R. M. E. (2019). Extensive Polygonal Fracture Network in Siccar Point group
1034 Strata: Fracture Mechanisms and Implications for Fluid Circulation in Gale Crater, Mars.
1035 *Journal of Geophysical Research: Planets*, 124(10), 2613–2634.
1036 <https://doi.org/10.1029/2019JE006125>
- 1037 Le Deit, L., Hauber, E., Fueten, F., Pondrelli, M., Rossi, A. P., & Jaumann, R. (2013). Sequence
1038 of infilling events in Gale Crater, Mars: Results from morphology, stratigraphy, and
1039 mineralogy: Sedimentary infilling in gale crater. *Journal of Geophysical Research:*
1040 *Planets*, 118(12), 2439–2473. <https://doi.org/10.1002/2012JE004322>
- 1041 **Léveillé et al., 2014**
- 1042 L’Haridon, J., Mangold, N., Fraeman, A. A., Johnson, J. R., Cousin, A., Rapin, W., David, G.,
1043 Dehouck, E., et al. (2020). Iron Mobility During Diagenesis at Vera Rubin Ridge, Gale
1044 Crater, Mars. *Journal of Geophysical Research: Planets*, 125(11).
1045 <https://doi.org/10.1029/2019JE006299>
- 1046 Mahaffy, P. R., Webster, C. R., Cabane, M., Conrad, P. G., Coll, P., Atreya, S. K., Arvey, R.,
1047 Barciniak, M., et al. (2012). The Sample Analysis at Mars Investigation and Instrument
1048 Suite. *Space Science Reviews*, 170(1–4), 401–478. [https://doi.org/10.1007/s11214-012-](https://doi.org/10.1007/s11214-012-9879-z)
1049 [9879-z](https://doi.org/10.1007/s11214-012-9879-z)
- 1050 Malin, M. C., & Edgett, K. S. (2000). Sedimentary Rocks of Early Mars. *Science*, 290(5498),
1051 1927–1937. <https://doi.org/10.1126/science.290.5498.1927>
- 1052 Mangold, N., Dehouck, E., Fedo, C., Forni, O., Achilles, C., Bristow, T., Downs, R. T.,
1053 Frydenvang, J., et al. (2019). Chemical alteration of fine-grained sedimentary rocks at
1054 Gale crater. *Icarus*, 321, 619–631. <https://doi.org/10.1016/j.icarus.2018.11.004>

- 1055 Martin, P. E., Farley, K. A., Baker, M. B., Malespin, C. A., Schwenzer, S. P., Cohen, B. A.,
1056 Mahaffy, P. R., McAdam, A. C., et al. (2017). A Two-Step K-Ar Experiment on Mars:
1057 Dating the Diagenetic Formation of Jarosite from Amazonian Groundwaters: A two-step
1058 K-Ar experiment on Mars. *Journal of Geophysical Research: Planets*, 122(12), 2803–
1059 2818. <https://doi.org/10.1002/2017JE005445>
- 1060 McAdam, A. C., Franz, H. B., Sutter, B., Archer, P. D., Freissinet, C., Eigenbrode, J. L., Ming,
1061 D. W., Atreya, S. K., et al. (2014). Sulfur-bearing phases detected by evolved gas
1062 analysis of the Rocknest aeolian deposit, Gale Crater, Mars: Rocknest sulfur phases
1063 detected by SAM. *Journal of Geophysical Research: Planets*, 119(2), 373–393.
1064 <https://doi.org/10.1002/2013JE004518>
- 1065 McAdam, A. C., Knudson, C. A., Sutter, B., Franz, H. B., Archer Jr, P. D., Eigenbrode, J. L.,
1066 Ming, D. W., Morris, R. V., et al. (2016). Reactions involving calcium and magnesium
1067 sulfates as potential sources of sulfur dioxide during MSL SAM evolved gas analyses.
1068 *Abstract #2277*.
- 1069 McAdam, A. C., Sutter, B., Archer, P. D., Franz, H. B., Wong, G. M., Lewis, J. M. T.,
1070 Eigenbrode, J. L., Stern, J. C., et al. (2020). Constraints on the Mineralogy and
1071 Geochemistry of Vera Rubin Ridge, Gale Crater, Mars, From Mars Science Laboratory
1072 Sample Analysis at Mars Evolved Gas Analyses. *Journal of Geophysical Research:*
1073 *Planets*, 125(11). <https://doi.org/10.1029/2019JE006309>
- 1074 **McLennan, S. M. (2014)**
- 1075 McLennan, S. M. and Grotzinger, J. P. (2008) The sedimentary rock cycle of Mars. In: J. F. Bell
1076 III (ed.) *The Martian Surface: Composition, Mineralogy, and Physical Properties*.
1077 Cambridge Univ. Press (Cambridge), pp. 541-577.
- 1078 Meyer, C. (2008) *The Martian Meteorite Compendium*,
1079 <http://curator.jsc.nasa.gov/antmet/mmc/index.cfm>
1080
- 1081 Milliken, R. E., Grotzinger, J. P., & Thomson, B. J. (2010). Paleoclimate of Mars as captured by
1082 the stratigraphic record in Gale Crater: Stratigraphy of Gale crater. *Geophysical Research*
1083 *Letters*, 37(4). <https://doi.org/10.1029/2009GL041870>
- 1084 Morris, R. V., Klingelhöfer, G., Schröder, C., Rodionov, D. S., Yen, A., Ming, D. W., de Souza,
1085 P. A., Wdowiak, T., et al. (2006). Mössbauer mineralogy of rock, soil, and dust at
1086 Meridiani Planum, Mars: Opportunity's journey across sulfate-rich outcrop, basaltic sand
1087 and dust, and hematite lag deposits: Iron mineralogy at meridiani planum. *Journal of*
1088 *Geophysical Research: Planets*, 111(E12), n/a-n/a.
1089 <https://doi.org/10.1029/2006JE002791>
- 1090 Morris, R.V., Rampe, E.B., Graff, T. G., Archer, P. D., Jr., Le, L., Ming, D. W., & Sutter, B.
1091 (2015). Transmission X-ray diffraction (XRD) patterns relevant to the MSL CheMin
1092 amorphous component: Sulfates and silicates. 46th LPSC, Abstract #2434, Houston, TX.

- 1093 Morris, R. V., Vaniman, D. T., Blake, D. F., Gellert, R., Chipera, S. J., Rampe, E. B., Ming, D.
1094 W., Morrison, S. M., et al. (2016). Silicic volcanism on Mars evidenced by tridymite in
1095 high-SiO₂ sedimentary rock at Gale crater. *Proceedings of the National Academy of*
1096 *Sciences*, 113(26), 7071–7076. <https://doi.org/10.1073/pnas.1607098113>
- 1097 Morris, R.V., Vaniman, D.T., Clark, J.V., Rampe, E.B., Ming, D.W., Achilles, C.N., and Archer,
1098 D.P. (2021). Toward understanding ferruginous smectite Mg for Ca interlayer cation
1099 exchange, crystalline Ca-sulfates, and amorphous Mg-sulfates on Mars. 52nd LPSC,
1100 Abstract #2548, Virtual.
- 1101 Morrison, S. M., Downs, R. T., Blake, D. F., Vaniman, D. T., Ming, D. W., Hazen, R. M.,
1102 Treiman, A. H., Achilles, C. N., et al. (2018). Crystal chemistry of martian minerals from
1103 Bradbury Landing through Naukluft Plateau, Gale crater, Mars. *American Mineralogist*,
1104 103(6), 857–871. <https://doi.org/10.2138/am-2018-6124>
- 1105 Mu, J., & Perlmutter, D. D. (1981). Thermal decomposition of inorganic sulfates and their
1106 hydrates. *Industrial & Engineering Chemistry Process Design and Development*, 20(4),
1107 640–646. <https://doi.org/10.1021/i200015a010>
- 1108 Murchie, S. L., Mustard, J. F., Ehlmann, B. L., Milliken, R. E., Bishop, J. L., McKeown, N. K.,
1109 Noe Dobra, E. Z., Seelos, F. P., et al. (2009). A synthesis of Martian aqueous
1110 mineralogy after 1 Mars year of observations from the Mars Reconnaissance Orbiter.
1111 *Journal of Geophysical Research*, 114, E00D06. <https://doi:10.1029/2009JE003342>
- 1112 Nachon, M., Clegg, S. M., Mangold, N., Schröder, S., Kah, L. C., Dromart, G., Ollila, A.,
1113 Johnson, J. R., et al. (2014). Calcium sulfate veins characterized by ChemCam/Curiosity
1114 at Gale crater, Mars: Calcium sulfate veins at gale crater. *Journal of Geophysical*
1115 *Research: Planets*, 119(9), 1991–2016. <https://doi.org/10.1002/2013JE004588>
- 1116 Nachon, M., Mangold, N., Forni, O., Kah, L. C., Cousin, A., Wiens, R. C., Anderson, R., Blaney,
1117 D., et al. (2017). Chemistry of diagenetic features analyzed by ChemCam at Pahrump
1118 Hills, Gale crater, Mars. *Icarus*, 281, 121–136.
1119 <https://doi.org/10.1016/j.icarus.2016.08.026>
1120
- 1121 Newsom, H., Belgacem, I., Jackson, R., Ha, B., Vaci, Z., et al. (2016). The materials at an
1122 unconformity between the Murray and Stimson formations at Marias Pass, Gale Crater,
1123 Mars. Lunar and Planetary Science Conference, Mar 2016, Houston, TX, United States.
- 1124 Rampe, E. B., Blake, D. F., Bristow, T. F., Ming, D. W., Vaniman, D. T., Morris, R. V.,
1125 Achilles, C. N., Chipera, S. J., et al. (2020). Mineralogy and geochemistry of sedimentary
1126 rocks and eolian sediments in Gale crater, Mars: A review after six Earth years of
1127 exploration with Curiosity. *Geochemistry*, 80(2), 125605.
1128 <https://doi.org/10.1016/j.chemer.2020.125605>
- 1129 Rampe, E. B., Bristow, T. F., Morris, R. V., Morrison, S. M., Achilles, C. N., Ming, D. W.,
1130 Vaniman, D. T., Blake, D. F., et al. (2020). Mineralogy of Vera Rubin Ridge from the
1131 Mars Science Laboratory CheMin Instrument. *Journal of Geophysical Research: Planets*,
1132 125(9). <https://doi.org/10.1029/2019JE006306>

- 1133 Rampe, E. B., Ming, D. W., Blake, D. F., Bristow, T. F., Chipera, S. J., Grotzinger, J. P., Morris,
1134 R. V., Morrison, S. M., et al. (2017). Mineralogy of an ancient lacustrine mudstone
1135 succession from the Murray formation, Gale crater, Mars. *Earth and Planetary Science*
1136 *Letters*, 471, 172–185. <https://doi.org/10.1016/j.epsl.2017.04.021>
- 1137 Rampe, E. B., Morris, R. V., Archer, P. D., Agresti, D. G., & Ming, D. W. (2016). Recognizing
1138 sulfate and phosphate complexes chemisorbed onto nanophase weathering products on
1139 Mars using in-situ and remote observations. *American Mineralogist*, 101(3), 678–689.
1140 <https://doi.org/10.2138/am-2016-5408CCBYNCND>
- 1141 Rapin, W., Ehlmann, B. L., Dromart, G., Schieber, J., Thomas, N. H., Fischer, W. W., Fox, V.,
1142 K., Stein, N. T., et al. (2019). An interval of high salinity in ancient Gale crater lake on
1143 Mars. *Nature Geoscience*, 12(11), 889–895. <https://doi.org/10.1038/s41561-019-0458-8>
- 1144 Rapin, W., Meslin, P.-Y., Maurice, S., Vaniman, D., Nachon, M., Mangold, N., Schröder, S.,
1145 Gasnault, O., et al. (2016). Hydration state of calcium sulfates in Gale crater, Mars:
1146 Identification of bassanite veins. *Earth and Planetary Science Letters*, 452, 197–205.
1147 <https://doi.org/10.1016/j.epsl.2016.07.045>
- 1148 Rice, M. S., Gupta, S., Treiman, A. H., Stack, K. M., Calef, F., Edgar, L. A., Grotzinger, J.,
1149 Lanza, N., et al. (2017). Geologic overview of the Mars Science Laboratory rover
1150 mission at the Kimberley, Gale crater, Mars: Overview of MSL at the Kimberley. *Journal*
1151 *of Geophysical Research: Planets*, 122(1), 2–20. <https://doi.org/10.1002/2016JE005200>
- 1152 Rivera-Hernández, F., Sumner, D. Y., Mangold, N., Banham, S. G., Edgett, K. S., Fedo, C. M.,
1153 Gupta, S., Gwizd, S., et al. (2020). Grain Size Variations in the Murray Formation:
1154 Stratigraphic Evidence for Changing Depositional Environments in Gale Crater, Mars.
1155 *Journal of Geophysical Research: Planets*, 125(2).
1156 <https://doi.org/10.1029/2019JE006230>
- 1157 Sheppard, R. Y., Milliken, R. E., Parente, M., & Itoh, Y. (2021a). Updated Perspectives and
1158 Hypotheses on the Mineralogy of Lower Mt. Sharp, Mars, as Seen from Orbit. *Journal of*
1159 *Geophysical Research: Planets*, 126(2). <https://doi.org/10.1029/2020JE006372>
- 1160 Sheppard, R. Y., Milliken, R. E., & Robertson, K. M. (2021b). *Presence of clay minerals can*
1161 *obscure spectral evidence of Mg-sulfates: Implications for orbital observations of Mars.*
1162 Presented at the 52nd Lunar and Planetary Science Conference, Abstract #1560.
- 1163 Siebach, K. L., Grotzinger, J. P., Kah, L. C., Stack, K. M., Malin, M., Lèveillé, R., & Sumner, D.
1164 Y. (2014). Subaqueous shrinkage cracks in the Sheepbed mudstone: Implications for
1165 early fluid diagenesis, Gale crater, Mars. *Journal of Geophysical Research: Planets*,
1166 119(7), 1597–1613. <https://doi.org/10.1002/2014JE004623>
- 1167 Sklute, E. C., Jensen, H. B., Rogers, A. D., & Reeder, R. J. (2015). Morphological, structural,
1168 and spectral characteristics of amorphous iron sulfates. *Journal of Geophysical Research:*
1169 *Planets*, 120(4), 809–830. <https://doi.org/10.1002/2014JE004784>

- 1170 Sklute, E. C., Rogers, A. D., Gregerson, J. C., Jensen, H. B., Reeder, R. J., & Dyar, M. D.
1171 (2018). Amorphous salts formed from rapid dehydration of multicomponent chloride and
1172 ferric sulfate brines: Implications for Mars. *Icarus*, 302, 285–295.
1173 <https://doi.org/10.1016/j.icarus.2017.11.018>
- 1174 Smith, R. (2021), “X-ray amorphous sulfur-bearing phases in sedimentary rocks of Gale crater,
1175 Mars - Supplemental”, *Mendeley Data*, V1, doi: 10.17632/8b5yj38wx3.1
- 1176 Smith, R. J., & Horgan, B. H. N. (2021). Nanoscale Variations in Natural Amorphous and
1177 Nanocrystalline Weathering Products in Mafic to Intermediate Volcanic Terrains on
1178 Earth: Implications for Amorphous Detections on Mars. *Journal of Geophysical*
1179 *Research: Planets*, 126(5). <https://doi.org/10.1029/2020JE006769>
- 1180 Smith, R. J., McLennan, S. M., Achilles, C. N., Dehouck, E., Horgan, B. H. N., Mangold, N.,
1181 Rampe, E. B., Salvatore, M., et al. (2021). X-Ray Amorphous Components in
1182 Sedimentary Rocks of Gale Crater, Mars: Evidence for Ancient Formation and Long-
1183 Lived Aqueous Activity. *Journal of Geophysical Research: Planets*, 126(3).
1184 <https://doi.org/10.1029/2020JE006782>
- 1185 **Smith, R. J. et al. (2018)**
- 1186 Stack, K. M., Grotzinger, J. P., Kah, L. C., Schmidt, M. E., Mangold, N., Edgett, K. S., Sumner,
1187 D. Y., Siebach, K. L., et al. (2014). Diagenetic origin of nodules in the Sheepbed
1188 member, Yellowknife Bay formation, Gale crater, Mars: Diagenetic Nodules in Gale
1189 Crater. *Journal of Geophysical Research: Planets*, 119(7), 1637–1664.
1190 <https://doi.org/10.1002/2014JE004617>
- 1191 Stein, N., Grotzinger, J. P., Schieber, J., Mangold, N., Hallet, B., Newsom, H., Stack, K. M.,
1192 Berger, J. A., et al. (2018). Desiccation cracks provide evidence of lake drying on Mars,
1193 Sutton Island member, Murray formation, Gale Crater. *Geology*, 46(6), 515–518.
1194 <https://doi.org/10.1130/G40005.1>
- 1195 Sun, V. Z., Stack, K. M., Kah, L. C., Thompson, L., Fischer, W., Williams, A. J., Johnson, S. S.,
1196 Wiens, R. C., et al. (2019). Late-stage diagenetic concretions in the Murray formation,
1197 Gale crater, Mars. *Icarus*, 321, 866–890. <https://doi.org/10.1016/j.icarus.2018.12.030>
- 1198 Sutter, B., McAdam, A. C., Mahaffy, P. R., Ming, D. W., Edgett, K. S., Rampe, E. B.,
1199 Eigenbrode, J. L., Franz, H. B., et al. (2017). Evolved gas analyses of sedimentary rocks
1200 and eolian sediment in Gale Crater, Mars: Results of the Curiosity rover’s sample
1201 analysis at Mars instrument from Yellowknife Bay to the Namib Dune. *Journal of*
1202 *Geophysical Research*, 122, 2574–2609. <https://doi.org/10.1002/2016JE005225>
- 1203 Swift, W. M., Panek, A. F., Smith, G. W., Vogel, G. J., & Jonke, A. A. (1976). *Decomposition of*
1204 *calcium sulfate: A review of the literature*. (ANL--76-122, 7224692; p. ANL--76-122,
1205 7224692). <https://doi.org/10.2172/7224692>
- 1206 Thompson, L. M., Berger, J. A., Spray, J. G., Fraeman, A. A., McCraig, M. A., O’Connell-
1207 Cooper, C. D., Schmidt, M. E., VanBommel, et al. (2020). APXS-Derived Compositional

- 1208 Characteristics of Vera Rubin Ridge and Murray Formation, Gale Crater, Mars:
1209 Geochemical Implications for the Origin of the Ridge. *Journal of Geophysical Research:*
1210 *Planets*, 125(10). <https://doi.org/10.1029/2019JE006319>
- 1211 Thomson, B. J., Bridges, N. T., Milliken, R., Baldrige, A., Hook, S. J., Crowley, J. K., Marion,
1212 G. M., de Souza Filho, et al. (2011). Constraints on the origin and evolution of the
1213 layered mound in Gale Crater, Mars using Mars Reconnaissance Orbiter data. *Icarus*,
1214 214(2), 413–432. <https://doi.org/10.1016/j.icarus.2011.05.002>
- 1215 Thorpe, M. T., Hurowitz, J. A., & Siebach, K. L. (2021). Source-to-Sink Terrestrial Analogs for
1216 the Paleoenvironment of Gale Crater, Mars. *Journal of Geophysical Research: Planets*,
1217 126(2). <https://doi.org/10.1029/2020JE006530>
- 1218 Tosca, N. J., Ahmed, I. A. M., Tutolo, B. M., Ashpittel, A., & Hurowitz, J. A. (2018). Magnetite
1219 authigenesis and the warming of early Mars. *Nature Geoscience*, 11(9), 635–639.
1220 <https://doi.org/10.1038/s41561-018-0203-8>
- 1221 Tosca, N. J., & McLennan, S. M. (2009). Experimental constraints on the evaporation of
1222 partially oxidized acid-sulfate waters at the martian surface. *Geochimica et*
1223 *Cosmochimica Acta*, 73(4), 1205–1222. <https://doi.org/10.1016/j.gca.2008.11.015>
- 1224 Tosca, N. J., McLennan, S. M., Clark, B. C., Grotzinger, J. P., Hurowitz, J. A., Knoll, A. H.,
1225 Schröder, C., & Squyres, S. W. (2005). Geochemical modeling of evaporation processes
1226 on Mars: Insight from the sedimentary record at Meridiani Planum. *Earth and Planetary*
1227 *Science Letters*, 240(1), 122–148. <https://doi.org/10.1016/j.epsl.2005.09.042>
- 1228 Treiman, A. H., Bish, D. L., Vaniman, D. T., Chipera, S. J., Blake, D. F., Ming, D. W., Morris,
1229 R. V., Bristow, T. F., et al. (2016). Mineralogy, provenance, and diagenesis of a potassic
1230 basaltic sandstone on Mars: ChemMin X-ray diffraction of the Windjana sample
1231 (Kimberley area, Gale Crater). *Journal of Geophysical Research: Planets*, 121(1), 75–
1232 106. <https://doi.org/10.1002/2015JE004932>
- 1233 Usui, T., Alexander, C. M. O., Wang, J., Simon, J. I., & Jones, J. H. (2012). Origin of water and
1234 mantle–crust interactions on Mars inferred from hydrogen isotopes and volatile element
1235 abundances of olivine-hosted melt inclusions of primitive shergottites. *Earth and*
1236 *Planetary Science Letters*, 357–358, 119–129. <https://doi.org/10.1016/j.epsl.2012.09.008>
- 1237 **VanBommel, S. J., (2016)**
- 1238 VanBommel, S. J., Gellert, R., Berger, J. A., Thompson, L. M., Edgett, K. S., McBride, M. J.,
1239 Minitti, M. E., Boyd, N. I., et al. (2017). Modeling and mitigation of sample relief effects
1240 applied to chemistry measurements by the Mars Science Laboratory Alpha Particle X-ray
1241 Spectrometer: Target relief effect mitigation and modeling for the MSL APXS. *X-Ray*
1242 *Spectrometry*, 46(4), 229–236. <https://doi.org/10.1002/xrs.2755>
- 1243 Vaniman, D. T. & Chipera, S. J. (2006). Transformations of Mg- and Ca-sulfate hydrates in Mars
1244 regolith. *American Mineralogist*, 91(10), 1628-1642. [https://doi-](https://doi-org.proxy.library.stonybrook.edu/10.2138/am.2006.2092)
1245 [org.proxy.library.stonybrook.edu/10.2138/am.2006.2092](https://doi-org.proxy.library.stonybrook.edu/10.2138/am.2006.2092)

- 1246 Vaniman, D. T., Bish, D. L., Chipera, S. J., Fialips, C. I., William Carey, J., & Feldman, W. C.
1247 (2004). Magnesium sulphate salts and the history of water on Mars. *Nature*, 431(7009),
1248 663–665. <https://doi.org/10.1038/nature02973>
- 1249 Vaniman, D. T., Bish, D. L., Ming, D. W., Bristow, T. F., Morris, R. V., Blake, D. F., Chipera,
1250 S. J., Morrison, S. M., et al. (2014). Mineralogy of a Mudstone at Yellowknife Bay, Gale
1251 Crater, Mars. *Science*, 343(6169), 1243480–1243480.
1252 <https://doi.org/10.1126/science.1243480>
- 1253 Vaniman, D. T., Martínez, G. M., Rampe, E. B., Bristow, T. F., Blake, D. F., Yen, A. S., Ming,
1254 D. W., Rapin, W., et al. (2018). Gypsum, bassanite, and anhydrite at Gale crater, Mars.
1255 *American Mineralogist*, 103(7), 1011–1020. <https://doi.org/10.2138/am-2018-6346>
- 1256 Wang, A., & Zhou, Y. (2014). Experimental comparison of the pathways and rates of the
1257 dehydration of Al-, Fe-, Mg- and Ca-sulfates under Mars relevant conditions. *Icarus*, 234,
1258 162–173. <https://doi.org/10.1016/j.icarus.2014.02.003>
- 1259 Wang, A., Freeman, J. J., & Jolliff, B. L. (2009). Phase transition pathways of the hydrates of
1260 magnesium sulfate in the temperature range 50°C to 5°C: Implication for sulfates on
1261 Mars. *Journal of Geophysical Research*, 114(E4), E04010.
1262 <https://doi.org/10.1029/2008JE003266>
- 1263 Wang, Y.-W., Kim, Y.-Y., Christenson, H. K., & Meldrum, F. C. (2012). A new precipitation
1264 pathway for calcium sulfate dihydrate (gypsum) via amorphous and hemihydrate
1265 intermediates. *Chem. Commun.*, 48(4), 504–506. <https://doi.org/10.1039/C1CC14210K>
- 1266 Watkins, J. A., Grotzinger, J., Stein, N., Banham, S. G., Gupta, S., Rubin, D., Stack, K. M., &
1267 Edgett, K. S. (2016). *Paleotopography of erosional unconformity, base of Stimson*
1268 *formation, Gale crater, Mars. Abstract #2939, 2.*
- 1269 Wiens, R. C., Maurice, S., Barraclough, B., Saccoccio, M., Barkley, W. C., Bell, J. F., Bender,
1270 S., Bernardin, J., et al. (2012). The ChemCam Instrument Suite on the Mars Science
1271 Laboratory (MSL) Rover: Body Unit and Combined System Tests. *Space Science*
1272 *Reviews*, 170(1–4), 167–227. <https://doi.org/10.1007/s11214-012-9902-4>
- 1273 Worden, R. H., & Burley, S. D. (2003). Sandstone Diagenesis: The Evolution of Sand to Stone.
1274 In S. D. Burley & R. H. Worden (Eds.), *Sandstone Diagenesis* (pp. 1–44). Blackwell
1275 Publishing Ltd. <https://doi.org/10.1002/9781444304459.ch>
- 1276 Yen, A. S., Ming, D. W., Vaniman, D. T., Gellert, R., Blake, D. F., Morris, R. V., Morrison, S.
1277 M., Bristow, T. F., et al. (2017). Multiple stages of aqueous alteration along fractures in
1278 mudstone and sandstone strata in Gale Crater, Mars. *Earth and Planetary Science Letters*,
1279 471, 186–198. <https://doi.org/10.1016/j.epsl.2017.04.033>
1280